# Application of micro-CT to deep-marine outcrop data: towards a new tool to better assess primary sedimentary structures and processes at their origin

Cornard, P.H [(1)] *, Degenhart, G. [(2)], Tropper, P. [(3)], Moernaut, J. [(1)], Strasser, M. [(1)]

[1]Institute of Geology, University of Innsbruck (Austria), Innrain 52, 6020, Innsbruck, Austria

[2]Department of Radiology, Core facility Micro CT, Medical University of Innsbruck, Christoph-Probst-Platz 1, Innrain 52 A, 6020, Innsbruck, Austria

[3]Institute of Mineralogy and Petrography, University of Innsbruck (Austria), Innrain 52, 6020, Innsbruck, Austria

*Corresponding author: P. H. Cornard, Department of Geology, University of Innsbruck, Innrain 52, Innsbruck, Austria. Email: pauline.cornard@uibk.ac.at.

This manuscript is a preprint and has been submitted for publication in The Depositional Record. The manuscript has not been peer-reviewed yet. Subsequent versions of the manuscript may thus contain slightly different content. Please feel free to contact the corresponding author directly to comment on the manuscript.

**ABSTRACT**

A new application of micro-CT on consolidated sediment-gravity flow deposits is presented with the objectives to characterize its internal sedimentary three-dimensional (3D) structures. The proposed concept is applied to three types of deep-marine sandstones, sampled in study areas showing different compositional properties: the Upper Cretaceous Gosau Group (Austria), the Eocene Hecho Group (Spain) and the Oligocene Annot Formation (France). From micro-CT data, the particle-size distribution is reconstructed in 3D, permitting a better visualization of the sedimentary structures showing distinct density contrast (grains versus matrix), most of the time, non-visible in 2D. Particle-size distribution show similar trend than grain-size computed from thin-section image analysis, testifying of the reliability of the micro-CT computed particle-size distribution. Because of the limitation of micro-CT to distinguish mineral phases, micro-CT data are complemented by micro-XRF and thin-section petrographic analysis. By separating particles based on their CT-density, it is possible to isolate the coarsest fraction underlying the sedimentary structures from the fine-grained matrix. Although some sedimentary structures do not appear visible from micro-XRF or thin-section analysis, due to too homogeneous mineral composition or grain size in the original flow or similar composition between matrix and grains, micro-CT techniques highlight internal sedimentary structures by isolating the coarsest fraction. This study brings into light (i) the potential of micro-CT and particle-size distribution in the analyses of sedimentary structures from outcrop data and related interpreted processes (sediment transport) and (ii) the importance to consider the mineralogical composition and the degree of grain sorting before to reach any interpretation of the processes at the origin of structureless deposits. Considering the importance of the sedimentary-structure visualization towards a reliable interpretation of processes at the origin of the deposits, micro-CT technique is a new and reliable tool to assess the physical properties of consolidated sandstones and read their internal sedimentary 3D structures.

Key words: micro-CT; sandstones; sedimentary structures; turbidites

## 1. INTRODUCTION

Over the last past several decades, medical X-ray computer tomography (CT) was widely used in the Earth Sciences, for imaging geological samples (Ketcham and Carlson, 2001). It has gained acceptance as a routine core analysis tool, highlighting the surface as well as the internal features, including bedding, sedimentary structures, fractures or cement distribution (e.g., Orsi et al., 1994; Baraka-Lokmane et al., 2009; Nelson et al., 2009; Penkrot et al., 2018). Although medical CT scanners have been significantly improved in terms of image quality and imaging speed, the spatial resolution stays limited to several hundreds of micrometers due to the size of the sample (e.g., meter-long core samples). Over the last decade, a new research domain developed in high-resolution X-ray tomography usually called micro-CT (e.g., Cnudde and Boone, 2013). Although micro-CT can only be applied to small samples (geological sample varying from 1 mm to 10 cm), the resolution is much higher than medical-CT, up to 2.5 µm. Since then, micro-CT techniques have been widely applied in Earth Sciences, especially in (i) 3D pore characterization (McCoy et al., 2006; Polacci et al., 2010) such as for reservoir characterization (Coenen et al., 2004; Sok et al., 2010; Tiwari et al., 2013; Kim et al., 2016; Schmitt et al., 2016; Lei et al., 2019; Su et al., 2022) and soil analysis (Sleutel et al., 2008; Munkholm et al., 2012; Singh et al., 2021); (ii) 3D grain analysis (Carlson, 2006; Jerram et al., 2009; Cnudde et al., 2011) particularly for minerals with metallurgical significance (Kyle and Ketcham, 2015; Ghorbani et al., 2011; Evans et al., 2015); (iii) structural processes (Otani et al., 2010; Siddiqui et al., 2010; Wildenschild and Sheppard, 2013), especially in fracture analysis (Bertels et al., 2001; Kumari et al., 2018; Yang et al., 2020). Without disregarding, the clastic sedimentology community also shows a growing interest in using micro-CT, particularly to highlight microfacies in sediment cores (Bendle et al., 2015; Van Daele et al., 2016; Wils et al., 2021; Sabatier et al., 2022). Despite this increased attention, there is a lack of study testing the potential of micro-CT to read internal primary sedimentary structures, especially on deep-marine consolidated sandstones.

Internal primary sedimentary structures of sediment-gravity flow (SGF) deposits are produced by physical processes during sediment transport and deposition (Middleton, 1965; Allen, 1970; Hiscott and Middleton, 1980; Arnott and Hand, 1989; Komar, 1989; Baas, 2004; Sumner et al., 2008; Talling, 2013). The recognition of primary sedimentary structures of SGF deposits provide key information about paleoflow conditions at the time of deposition. In the depositional record, primary sedimentary structures are rendered visible by variations in grain size (e.g., grading, sorting) and/or mineral composition (e.g., higher concentration of clay, micas or organic matter) within the lamination set (Kuenen, 1966; Campbell, 1967; Paola et al., 1989; Cheel, 1990; Best and Bridge, 1992). Although internal sedimentary structures of consolidated SGF deposits are well recognized in the rock record (e.g., Kiminami and Kontani, 1979; Stow and Piper, 1984; Stevenson et al., 2020) and reproduced in flume-tank experiments (e.g., Arnott and Hand, 1989; Sumner et al., 2008; Cartigny et al., 2013) and by numerical modelling (e.g., Jiang, 1995; Legros, 2002), there is a lack of characterization of these structures in three dimensions (3D) and at the micro-scale.

This study aims to discuss the potential of micro-CT to read internal primary sedimentary structures of consolidated SGF deposits. Because of (i) the importance of the mineral composition and the post-depositional processes (i.e., diagenesis) in the visualization and preservation of the sedimentary structures and (ii) the limitation of micro-CT to distinguish mineral phases, micro-CT analysis are complemented by chemical analysis including micro X-ray fluorescence (micro-XRF) and thin-section petrographic analysis. To better highlight the grain fabric within the sedimentary structures, particle-size is directly computed from micro-CT data. This multi-technique approach is applied on SGF deposits with contrasting mineral composition outcropping in ancient deep-marine formations: the Upper Cretaceous Gosau Group (Austria), the Middle Eocene Hecho Group (Spain) and the Late Eocene-Early Oligocene Annot Formation (France).

We wish to show in this paper that micro-CT technique (and related computed particle size) in conjunction with chemical analysis provide an innovative and accurate method in reading sedimentary 3D structures of consolidated SGF deposits. *In fine*, this approach aims to bring key answers to a fundamental and common interest of sedimentologists related to the reconstruction of paleoflow conditions responsible for the deposition of ancient deposits.

## 2. METHODS

### 2.1 Fieldwork

Samples were collected in three study areas showing different mineral composition: the Upper Cretaceous Gosau Group (Austria) showing a high content in dolomite, the Middle Eocene Hecho Group (Spain) with a high carbonate content, and the Oligocene Annot Formation characterized by a low content in carbonate. Each sample was collected in beds interpreted as low-density turbidites (see Pickering and Hiscott, 2016, for definition) and showing different types of internal sedimentary structures.

The Upper-Cretaceous Gosau Group is a synorogenic, siliciclastic sedimentary system that was deposited in the Muttekopf Basin that crops out in the Northern Calcareous Alps of the Eastern European Alps (Fig. 1A). The Gosau Group in the Muttekopf Basin (Western Austria) are preserved in a syncline in the hanging wall of the Inntal Nappe, composed of the Hauptdolomite Triassic carbonate shelf (Wagreich and Faupl, 1994). In the field, the sample (called Gosau sample in this study) was collected within the Megasequence 2 (Ortner, 2001), and retrieved in a thin-bedded sandstone showing a normal grading and a structureless base overlain by planar-parallel lamination (Fig. 1B).

The Hecho Group represents an accumulation of ~ 4 km of Middle Eocene deep-marine siliciclastic sediments infilling the South Pyrenean foreland Ainsa and Jaca basins (Mutti et al.,

1977) (Fig. 1C). The sample (called Hecho sample in this study) was collected in the Ainsa Basin, and more precisely in the Ainsa System in the outcropping Ainsa Quarry. The sample was retrieved in a normal graded medium-bedded structureless sandstone with a sharp base (Fig. 1D).

The Tertiary Grès d'Annot Formation of South East France is a Late Eocene-Early Oligocene sand-rich deep-marine system deposited in a wedge-top basin as part of a foreland system developed in front of the Alpine Orogen (Pickering and Hilton, 1998). The Grès d'Annot Formation is preserved in isolated areas termed "sub-basins". The sample (called Annot sample in this study) presented in this study was collected in the Annot sub-basin (Fig. 1E), and more precisely on a normal-graded thin-bedded sandstone showing planar-parallel lamination overlain by ripple-cross and convolute lamination (Fig. 1F).

The paleoflow direction is marked on each sample. Paleoflow was interpreted in the field based on flute casts or from the orientation of ripple-cross lamination.

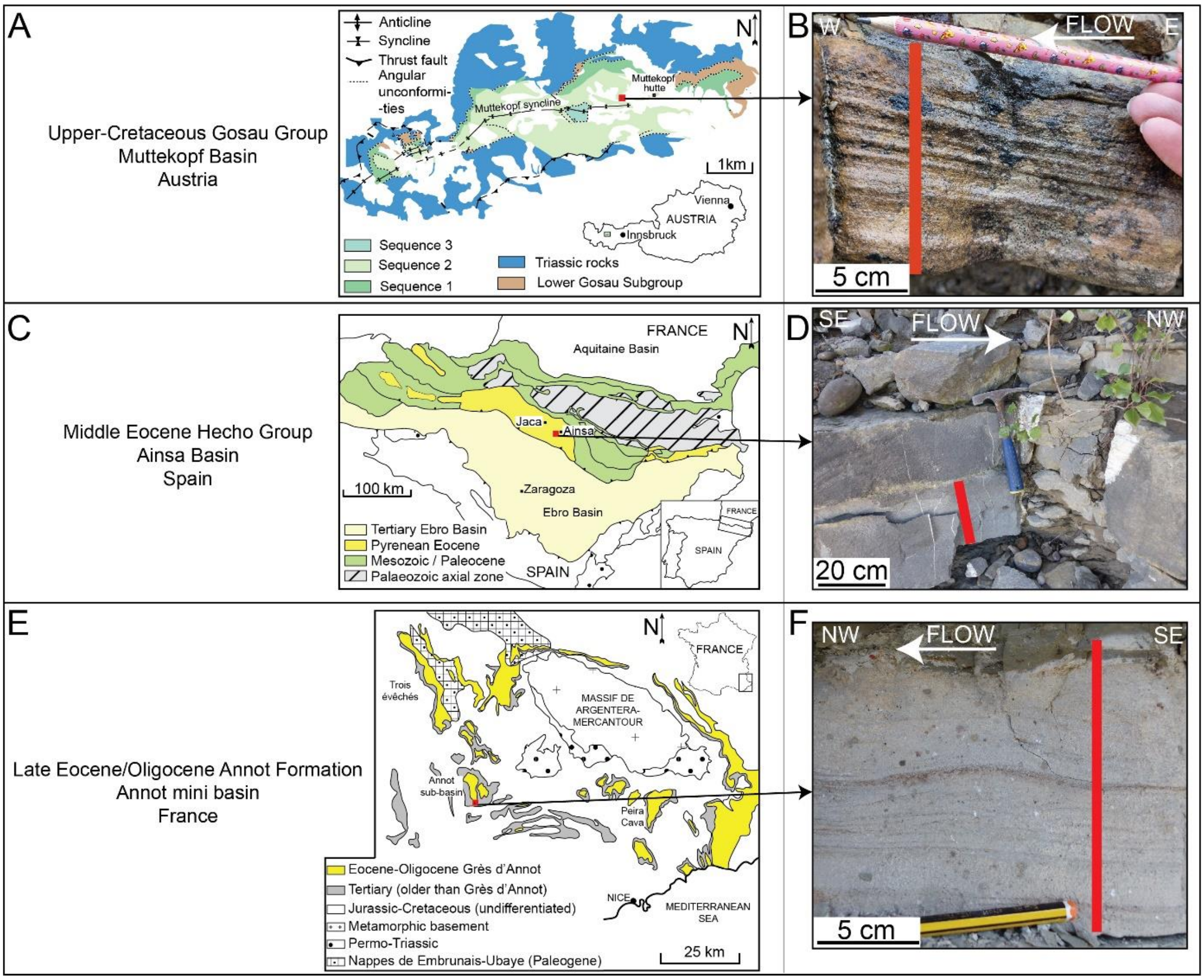


Figure 1: **(A)** Simplified geological map of the Upper-Cretaceous Gosau Group in the Muttekopf Basin (modified from Ortner et al., 2016). Red square indicates the sample location. **(B)** Turbidite of the Upper-Cretaceous Gosau Group in which sample was taken. Red line indicates the coring location. **(C)** Simplified geological map of the South Pyrenean foreland basin, including the Ainsa and Jaca basins filled by the Middle Eocene Hecho Group deposits (modified from Vergès et al., 2002). Red square indicates the sample location. **(D)** Turbidite of the Hecho Group (Ainsa Quarry) in which sample was taken. Red line indicates the coring location. **(E)** Simplified geological map of the Grès d'Annot Formation of South East France (modified from Pickering and Hilton, 1988). Red square indicates the sample location. **(F)** Turbidite of the Grès d'Annot Formation (Annot sub-basin) in which sample was taken for this study. Red line indicates the coring location.

## 2.2 Sample preparation and workflow

Sample collected in the field (Fig. 2 – step 1) were drilled with a 12 mm diameter drill bit (Fig. 2 – step 2) in order to fit in the micro-CT holding device (vivaCT40). The coring technique was chosen as rounded samples are more suitable for micro-CT analyses than samples with sharp edges producing significant artefacts. In the micro-CT scanner, samples were always oriented in the same direction, following the plane parallel to the paleoflow direction. Micro-CT data are used (i) to evaluate the internal 3D structures of the samples based on the CT density contrast between the different minerals and, (ii) to compute the particle-size distribution through the sample in 3D.

Once micro-CT data were collected, core samples were cut in half in order to apply micro-XRF on a plane surface (Fig. 2 – step 3). Because grains are usually oriented in specific directions with respect to the paleoflow (e.g., Hiscott and Middleton, 1980; Arnott and Hand, 1989), samples were cut parallel to the paleoflow direction in order to get the most of the flow characteristics. Cut surfaces were gently polished with a sand paper to increase quality of micro-XRF maps. However, we tried to limit the polishing in order to not jeopardize the alignment between micro-XRF map and thin-section image. Micro-XRF analysis gives an overview in the chemical element distribution through the sample. After alignment between micro-CT and micro-XRF images and by combining chemical elements together in the micro-XRF maps, it is possible to label the minerals in the micro-CT and to get an overview of their distribution through the sample and within sedimentary structures.

Thin-sections were cut on the surface plane of the half core in order to do a direct comparison between the micro-XRF data and thin-section pictures (Fig. 2 – step 4). High-resolution pictures of the thin-sections were taken for each sample with the aim to undertake analysis of the grain-size distribution by thin-section image analysis.

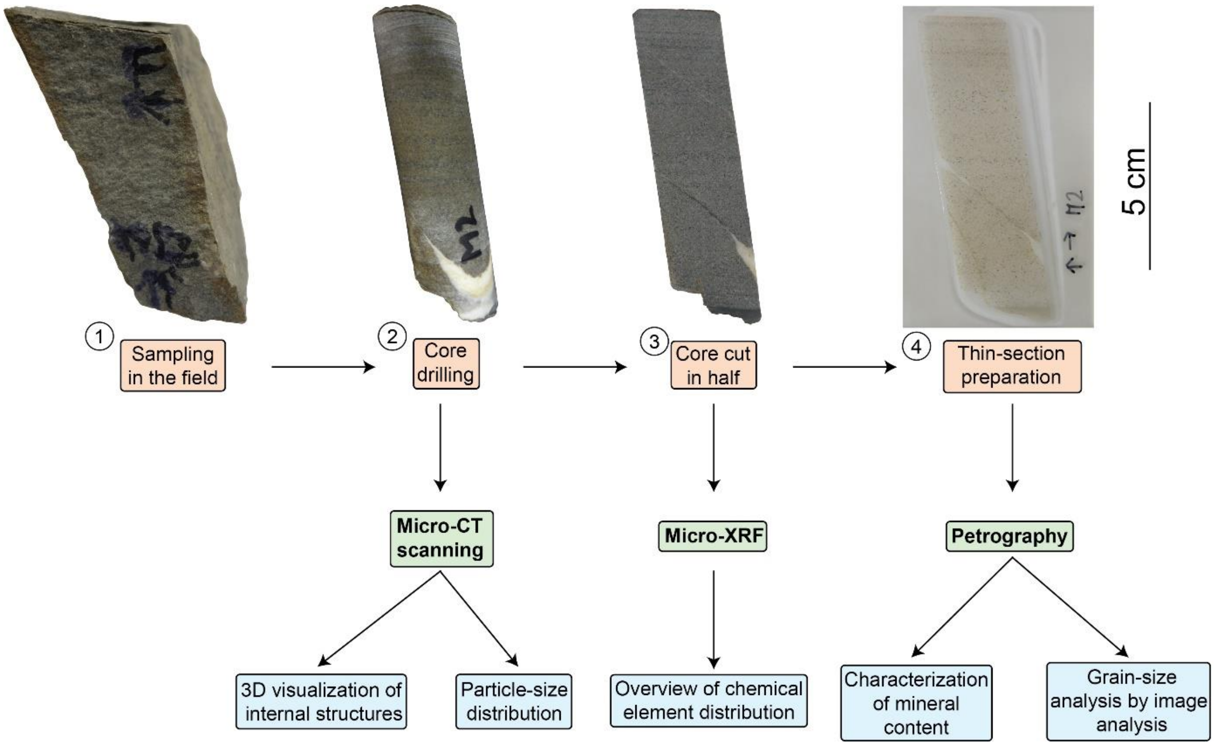


Figure 2: Workflow of the methodology adopted in this study.

### 2.3 Micro-CT

Micro CT imaging was performed using a vivaCT 40 (Scanco Medical AG, Brüthisellen CH) at the Medical University of Innsbruck. The vivaCT 40 is based on the cone beam geometry developed by Feldkamp et al. (1989). Thus, being a quantitative CT, the vivaCT 40 does not represent image grayscales using the Hounsfield unit scale as medical CT does, but is using the density of hydroxyapatite $Ca_{10}(PO_4)_6(OH)_2$(HA) resulting in grayscales following a scale of mgHA/ccm3. The scanning parameters were set in consideration to resolutions and image quality (signal to noise ratio, occurrence of image artefacts). Scanner settings for the examinations were a voltage of 70kV, a 114µA current, an integration time of 600ms, and a field of view of 21,5 mm resulting in a 1024x1024 image matrix with a resolution of 21 µm due to hardware binning of 2 in the detector. Thus, the potential minimum resolvable grain size is around 40 µm.

## 2.4 Image processing

Image post processing and visualization was performed using the Scanco Medical software suite provided for micro-CTs in combination by Image Processing Language (IPL; Institute for Biomedical Engineering ETHZ, University of Zürich; Rüegsegger, et al., 1996). For the evaluation of the particle size, a standardized procedure was developed (Fig. 3):

1. Selection of the volume of interest (VOI) (in some cases contouring of the VOI)
2. Noise reduction using a Gaussian convolution filter (settings sigma: 1.6 and support: 3)
3. Evaluation of thresholds
4. Performing threshold segmentation steps
5. Calculation of global structural parameters
6. Calculation of slice wise structural parameters (particle size)

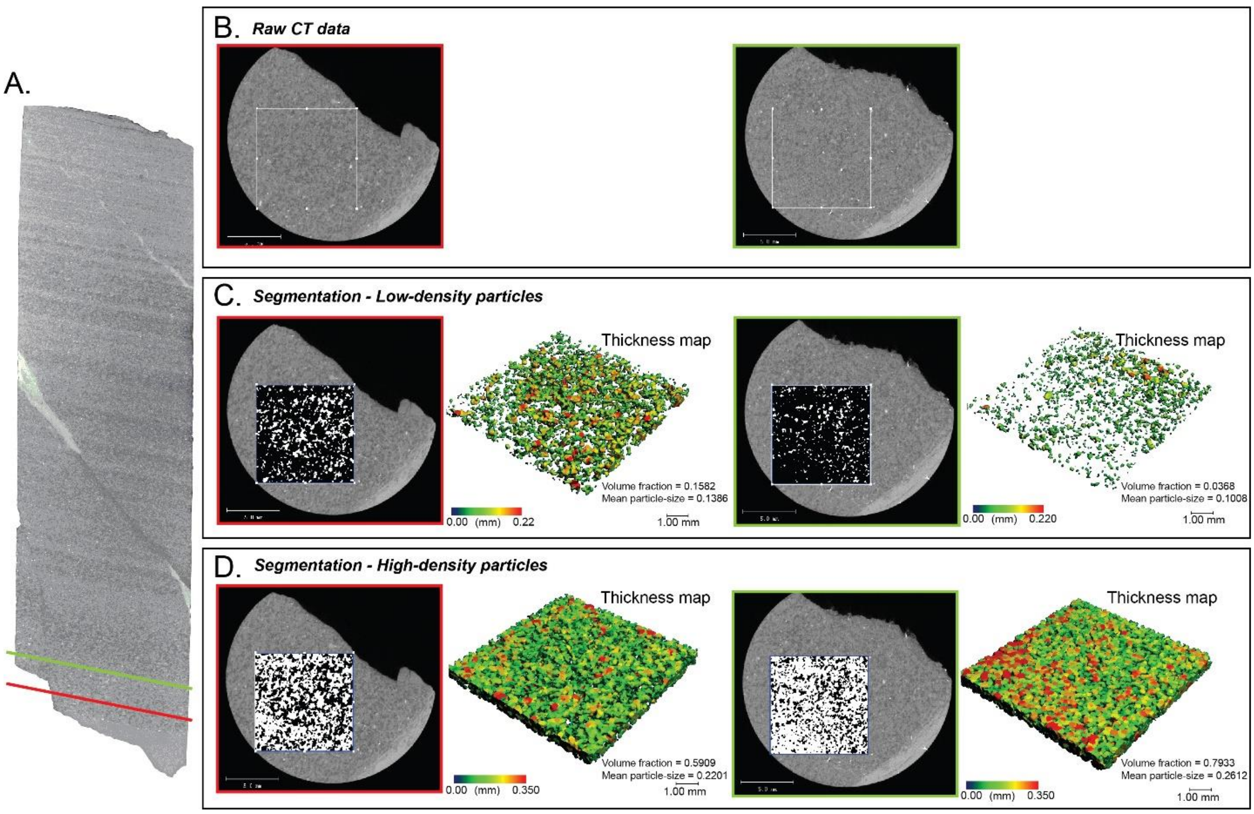

Figure 3: **A.** Visualization of micro-CT native image in longitudinal view with two layers of different composition marked in green and red (marked layers in B, C, and D). **B.** Axial view in the two marked layers with the contour for the evaluation marked; additionally, noise reduction was applied. **C.** Segmentation and false color codes imaging of low-density particle distribution in the two layers. **D.** Segmentation and false color codes imaging of high-density particle distribution in the two layers.

#### *2.4.1. Contouring of the outline of the VOI*

For samples where an evaluation of the whole volume is necessary, a multi-step process was established using basic image manipulation algorithms implemented in IPL. This method is needed in cases where holes in the sample occur. In the first step, a rough contour is drawn around the sample. In the next step, thresholding is performed containing all the materials scanned except gases. The binarized result is then dilated by 5 voxels closing small holes and channels from the inside of the sample to the surroundings. In the next step, the image gets inverted having the effect that holes are now objects in the segmented space, which can be distinguished using component labelling. Under the assumption that due to the rough segmentation, the biggest component is the outside of the sample after the inverting of the image space, it is now possible to cut off all smaller volumes (holes). This result is inverted again, eroded by 5 voxels and transferred into a contour file representing now the outer contour of the object but containing all the gas filled holes. For this study, this was applied to the sample of Gosau but not for Annot and Hecho samples (due to too large sample volume and, thus an overflow of memory) where only a squared VOI inside the sample was analyzed.

#### *2.4.2. Threshold estimations*

Guided by Boone et al. (2011) and Bam et al. (2020) that the linear attenuation of x-rays is connected to the atomic number of elements, the mass density of the analyzed material and by the guiding mineral, assumptions for grayscale domains being correlated to certain mineral compositions must be seen as valid. Combining this assumption with the mineral resolution of micro-XRF analysis, a rough estimation of the linear attenuation in CT for mineral compounds is indirectly possible. Aligning the micro-CT images with the analyzed micro-XRF (Fig. 4), plane correlations between silicate-dominated lamination and carbonate-dominated lamination become visible. Visual analysis of the micro-CT high-density areas can be matched with carbonate-rich domains. Further single high-density particles can also be distinguishing from other potential mineral compositions, although there is a possible overlap in the CT density. This practice is easily applied and modified to changes in mineral composition.

For thresholding, the base grayscale space of 16 Bit is rescaled to 1000 steps to make the manual adaption easier. Based on these observations and the knowledge that samples are sandstones, three grayscale domains were selected representing low-, middle- and high-density particles as they best describe the mineral information and the grayscale phases seen in the micro-CT images. As base value for the low threshold, a window of 423-1084 mgHA/ccm$^3$ is assumed. The middle window ranges from 1085 to 1458 mgHA/ccm$^3$.The high window varies from 1459 to 2378 mgHA/ccm$^3$. The 2379-2666 mgHA/ccm$^3$ window is not considered because it normally correlates to high-density minerals (e.g., pyrite). These high-density minerals have the disadvantage of having hard artefacts around its borders with the used machine settings and therefore are not detectable properly. For each sample, these basic threshold windows had to be adapted minimally because of the occurrence of partial volume effects and possible changes in the composition of the mineral domains. This modification was made subjective based on the visibility of particles in the micro-CT images.

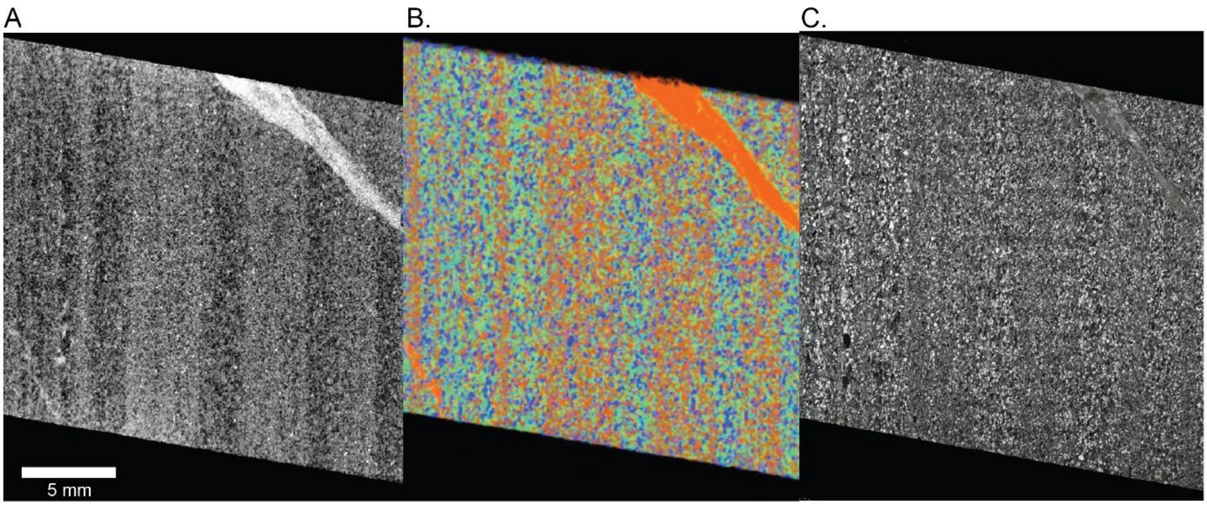


Figure 4: Alignment between micro-CT, micro-XRF and thin section (example taken from the Gosau sample). **A.** Micro-CT image with optimized image contrast (dark colors: low-density particles; light colors: high-density particle). **B.** Micro-XRF image (Green: Silica; Blue: Aluminum; Orange: Calcium). **C.** Thin section image.

### *2.4.3 Calculation of structural parameters*

Each thresholding result is separately fed into the calculation pipeline where stepwise volumetric density and structural parameters are evaluated. Following parameters are evaluated for each sample slicewise and as a measure for the whole volume:

- Volumetric parameters: the total volume of the analysis, the volume of the segmented material, and the volume fraction of the segmented material to the whole volume.
- Density parameters: the mean density of the material is calculated represented in mgHA/ccm$^3$
- Particle size: under the assumption that areas with the same density window are composed of the same material composition, the particle size is calculated by a bubble-growing algorithm introduced by Hildebrand and Rüeggsegger (1997).

### *2.4.4 Particle size*

Particle size is calculated, as mentioned, by the algorithm implemented by Hildebrand and Rüeggsegger (1997). The original usage of this algorithm was targeted at the mean thickness of bone trabecular structures. The basic paradigm of the algorithm is based on the assumption of growing virtual bubbles within a segmented volume. As soon as the bubble hits two edges, the short axis of a certain structure is reached. This step is to be repeated until all voxels inside the analyzed sample are labeled by at least one bubble object. In the next step, the labels of each voxel are sorted by size and only the biggest label defines the bubble diameter (Fig. 5). In the next step, the diameter of each voxel gets read out and the mean value is calculated, resulting in the mean size of the particle. Using IPL, it is possible to quantify the result of the particle size for not only the whole volume but also for the slicewise features. Slicewise features are, then, exported into a table using the *zmean* command. This assumption is transformed to the short axis analysis of diameters of particles.

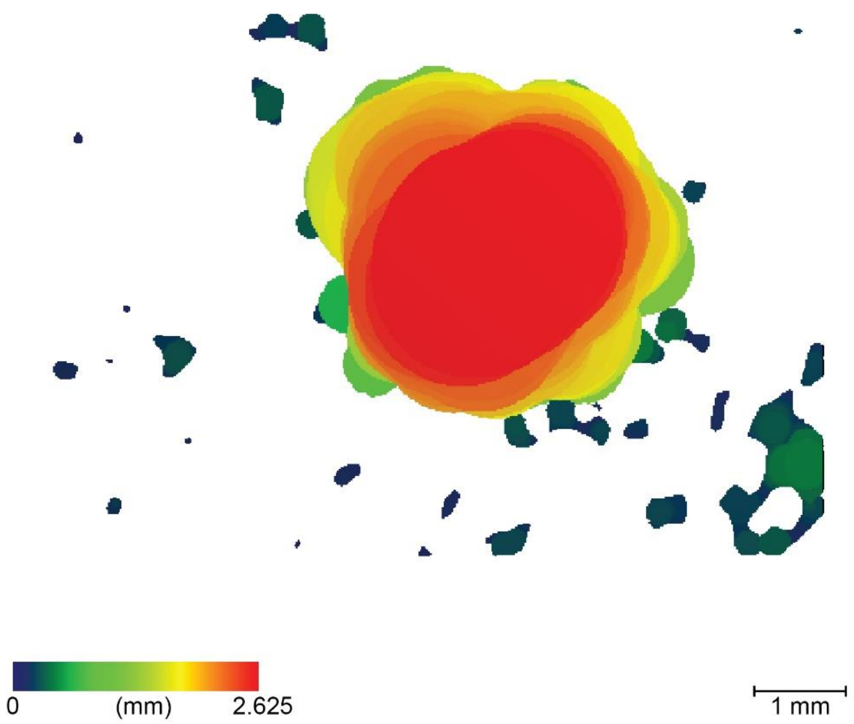

Figure 5: Result of a slicewise extraction for the diameter of a particle. Color code represents the highest value of each voxel contributing to the final measured diameter of a particle.

## 2.5 Micro-XRF

Non-destructive micro-XRF analyses were carried out using a Bruker M4 Tornado at the Institute of Mineralogy and Petrography of the University of Innsbruck. The Bruker M4 Tornado uses a single rhodium target X-ray tube with up to 50 kV and 600 µA power and equipped with a Be window, focusses the beam with polycapillary optics down to a spot size of ~25 µm. However, because of the computer running out of memory due to large-size sample, the spot-size was fixed at 50 µm for the Gosau and Hecho samples and 70 µm for the Annot sample. This microanalytical instrument provides element mapping of the entire sample via the x-y-z moving stage. Maps of chemical element distribution is visualized using the function of "area analysis mapping" of the Brucker M4 Tornado software. By layering chemical elements together, it is possible to interpret mineral phases and to get an overview of the mineral distribution through the sample. This was later confirmed by mineral identification in thin sections.

## 2.6 Thin-section

Thin sections, cut on the surface plane where micro-XRF was measured, have a standard thickness of 30 µm and were soaked in an epoxy resin. Thin-sections cover the entire low-density turbidite (from the base to the top) for the Gosau sample. However, the sample of the Hecho and Annot had to be cut in two as it was too long to fit in a single thin section. Main mineral phases, matrix composition and the potential presence of cement were characterized by the analyses of thin-section with a transmitted light optical microscope.

## 2.7 Grain-size analysis by thin-section image analysis

Images of thin sections were acquired using the microscope Zeiss Axio Imager A1m and the high-resolution IMAGINGSOURCE DFK33UX264 camera giving image with resolution of 3616 dpi, and thus a technical resolution up to ~ 7 µm. Pictures were acquired automatically using the software Petrog 5.0.3.5 along with a moving stage. To avoid any problems during stitching, a 10% overlap was setup between each picture. Pictures were stitched together using Imagej (version 1.53q) software. Image processing procedures were implemented using Imagej and Matlab to separate the grains from the matrix (segmentation) and to evaluate the 2D grain-size distribution throughout the sample, respectively. To be consistent with the evaluation of particle size computed from micro-CT data, the grain-size from image analysis of thin-sections is based on the short-axis of a grain. Each stitched image of thin section was converted to a greyscale (8-bit image). Noise was reduce using filters such as "Median" replacing each pixel with the neighborhood mean. In order to improve the image segmentation, contrast was enhanced in the pictures. Threshold was later applied in order to produce a binary image. For each thin-section image, two binary images were produced. A first one isolating the darkest grain such as clay or some feldspar, and a second binary image with the lightest grains including quartz, carbonate and feldspar. Using the plugin MorpholibJ in ImageJ, a distance transform watershed map was created, to separate the touching grains in the best possible way. Grain discretization was improved by multiplying the original binary image by the distance transform watershed map. From the resulting map, the value of the short-axis of each grain along with its coordinates were exported using the MorpholibJ plugin in ImageJ. The grain-size data measured with ImageJ was analyzed using the Matlab *grainmap* code from Falvard and Paris (2017) giving a grain-size map of the sample. The grain-size and color bar scale were modified in order to fit the dataset. This permits a 2D visualization of the grain-size distribution and structures along the sample.

## 3. TERMINOLOGY

*Sedimentary structures* – Sedimentary structures are generated from materials of different compositions and are products of physical (sediment transport), chemical (e.g., chemical reactions between particles) and biological processes (animal or plant life modifying sediments) (e.g., Collinson, 2019 and references therein). In this study, we refer to primary sedimentary structures to the ones related to sediment transport. The correct interpretation of primary sedimentary structures permits to unravel processes at their origin. If physical conditions or sediment supply vary through time during ongoing flow, laminae of sediment with different character are deposited (Campbell, 1967). The resulting deposit will present set of laminae (lamination) with contrasting compositional and textural properties, making the internal sedimentary structures visible with the naked eye. Examples of primary sedimentary structures typically observed in deep-marine sandstones are ripple-cross lamination, planar-parallel lamination or cross lamination.

*Grains vs particles* – We refer to grains to the basic coarsest components of sandstones. This includes detrital grains such as quartz, feldspar, calcite or dolomite. “Particles” in comparison to “grains” are seen as areas formed from homogeneous CT density distribution. The term “particle” is only used in analysis of CT data. Grains with touching edges, a size below the CT-resolution (silt) and showing a homogeneous density distribution are seen as a single interconnected particle. In this case, and especially for the matrix component, the particle size might be coarser than the real grain size, due to the algorithm considering several very-small size interconnected grains as one particle.

*Matrix* – The fine-grained component (<silt size) filling the spaces between the detrital grains is referred to the matrix. Matrix is commonly composed of clay minerals mixed with silt-sized calcite, dolomite, quartz or feldspar. In this paper, we also considered the cement part of the matrix as it cannot be distinguished with micro-CT techniques.

# 4. RESULTS

## 4.1 Upper-Cretaceous Gosau sample

### ***Observed micro-CT characteristics***

Micro-CT results of the sample from the Gosau Formation (Fig. 6A) show a progressive decrease in the distribution of low-density particles (dark particles) from the base of the sample to the top of the sample (Fig. 6B). The first centimeters at the base, mainly composed of low-density particles, do not show particular organization. The sample is mainly characterized by an alternation of low- and high-density particles forming millimeter-scale laminae (up to 5 mm thick) throughout the sample. The micro-CT image clearly highlights a decrease in the laminae thickness from the base to the top of the sample.

### ***Computed particle-size variation***

Three density thresholds are defined (Fig. 6C). The highest density threshold ranges from 1605 to 2378 mgHA/ccm$^3$. It shows a volume fraction of 0.025 and a mean particle size of 0.4725 mm (Table 1). High-density particles partially highlight the sedimentary structures, however, it is in a minor proportion. High-density particles are mainly infilling the fracture crossing through the sample (Fig. 6D). The significant variation in the high-density particle size observed in the graph in figure 6C is related to the presence of the fracture infill, in which, large-size particle is computed because of the limit of the algorithm to calculate particle dimension lower than silt size (See Discussion section 5.4).

The middle-density threshold, ranging from 1189 to 1604 mgHA/ccm$^3$, has a mean particle size of 0.3221 mm and a volume fraction of 0.7489 (Table 1). Middle-density are most likely related to the matrix (Fig. 6E). In some case where the matrix is mainly composed of silt-size particles below the resolvable resolution of 40 µm (see Discussion section 5.4) and with the same CT-density, the algorithm cannot distinguish the particle edges (interconnected particles) and computes coarse-size particles. This is mainly observed on the sample edges (Fig. 6E). This is considered as an artefact and should not be considered in the analysis of particle-size distribution. It also results in a relatively large particle size as observed in the graph in figure 6C.

The low-density threshold, ranging from 423 to 1188 mgHA/ccm$^3$, shows a volume fraction of 0.1796 with a mean particle size of 0.136 mm (Table 1). Low-density particles underlined internal structures showing planar-parallel lamination with a lamination thickness as well as a particle-size decreasing towards the top of the sample (Fig. 6F). Sedimentary structures are well highlighted by the variation in particle size and volume fraction of the low-density particles as observed in figure 6C.

From the alignment between micro-CT and micro-XRF, the low-density particles correspond to silicate fraction (e.g., quartz and feldspar) whereas the middle-density particles are related to the mixture of silicate and carbonate fractions, mainly forming the matrix. The high-density particles are related to the carbonate fraction and especially to calcite as shown by the infill of the fracture.

***Micro-XRF***

Two chemical-element assemblages are observed. The first one mainly located at the base of the sample and underlying the lamination throughout the sample, is made of silica and potassium (pink/yellow lamination in Fig. 6G). By layering these chemical elements, these laminations are deduced to be composed of the minerals quartz (pink), K-feldspar (yellow) and clay (orange). On the contrary, thicker laminae showing a high content of magnesium, silica and calcium are deduced to be mainly composed of dolomite (brown) and clay (orange), which is most likely related to the matrix composition. This is confirmed by other chemical elements in Supplementary 1 and comparison with petrographic analysis of thin section.

***Petrography and grain-size distribution***

Sandstone sample of the Gosau Formation consists of a poorly sorted arenite. Quartz minerals are dominant and a significant amount of alkali feldspar are observed (Fig. 7). Micas and plagioclase are common and carbonate minerals are rare. Clay flocks are abundant and their amount increase towards the top of the sample. Grains are sub-angular to sub-rounded. A fine-grained micritic carbonate matrix is filling the space between the larger detrital grains. Some quartz and feldspar are surrounded by a calcite cement (Fig. 7).

Grain-size analysis by image analysis of thin-section gives a grain-size up to 0.50 mm (grain short axis). Mean grain-size calculated for the light-grain fraction is 0.0450 mm. Mean grain-size computed for the dark-grain fraction is 0.0476 mm (Table 1). A general fining upward trend is observed. Grain-size segregation is seen between the lamination forming the internal structures of the sample (Fig. 6I).

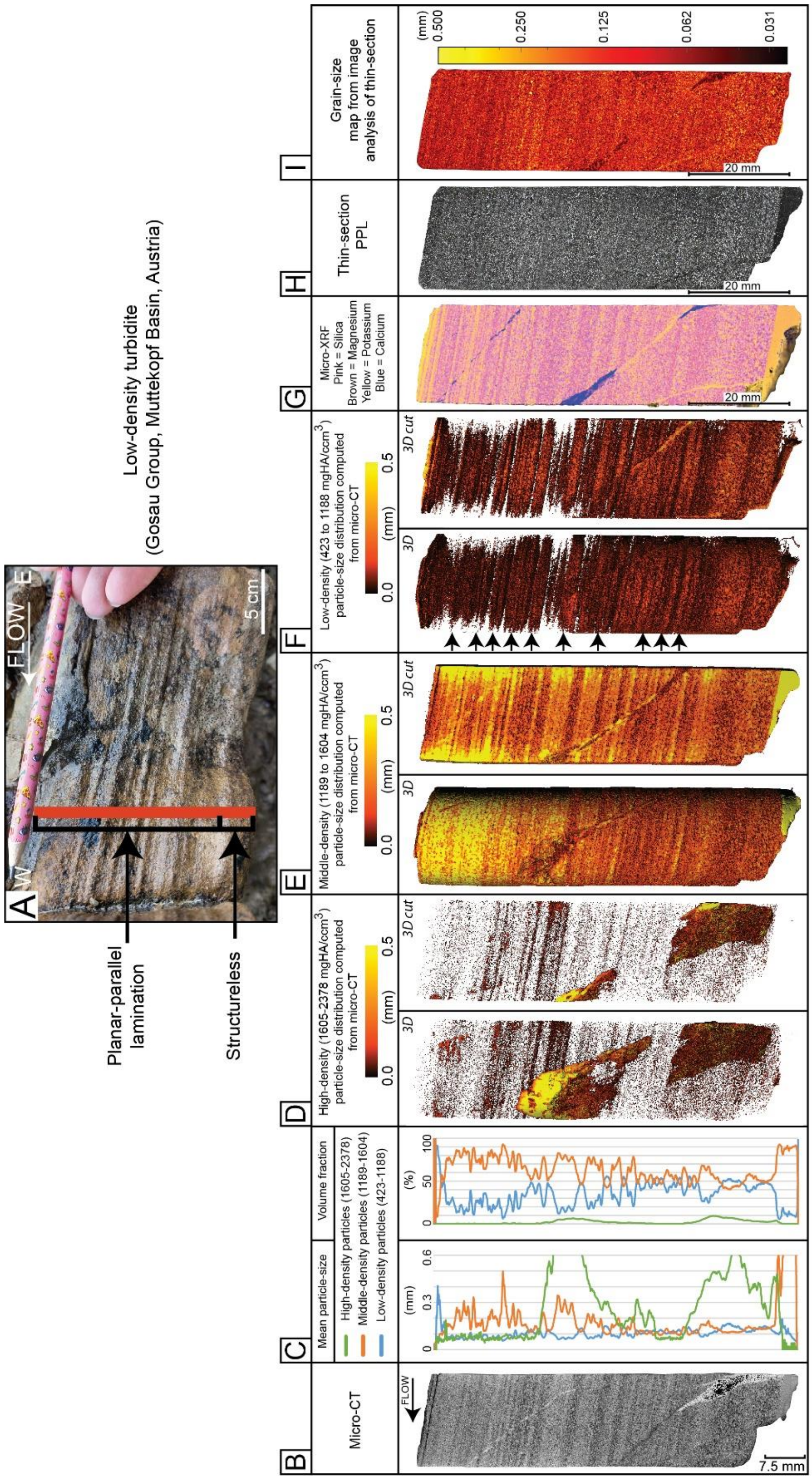


Figure 6: **(A)** Turbidite sampled in the Upper-Cretaceous Gosau Group showing structureless base overlain by planar-parallel lamination. **(B)** Native micro-CT image. Dark colors: low-density particle; light colors: high-density particles. **(C)** Graphs illustrating the variations of computed particle-size and volume fraction along the sample for each CT-density threshold.

**(D)** Distribution of high-density computed particle-size in 3D and in a 3D cut parallel to the paleoflow direction. **(E)** Distribution of middle-density computed particle-size in 3D and in a 3D cut parallel to the paleoflow direction. **(F)** Distribution of low-density computed particle-size in 3D and in a 3D cut parallel to the paleoflow direction. Arrows indicate sedimentary structures. **(G)** Micro-XRF map. **(H)** Thin-section image (PPL = plain-polarized light). **(I)** Grain-size map computed from thin-section image analysis.

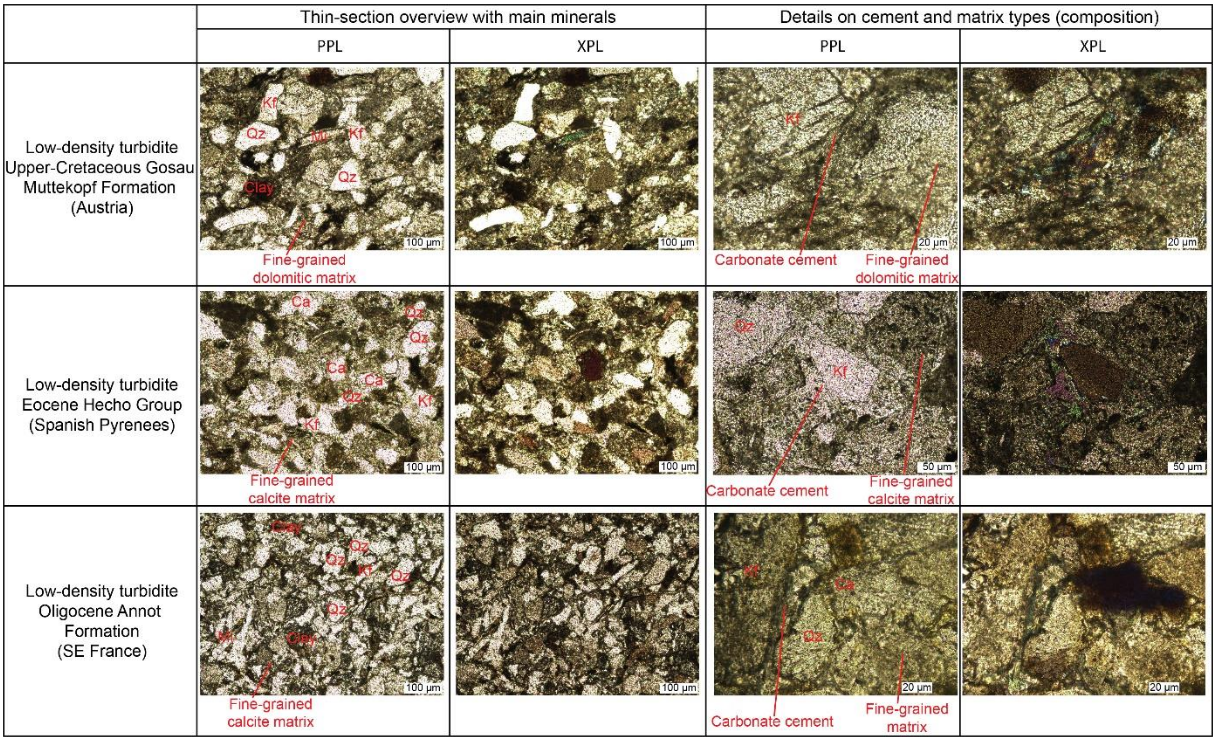


Figure 7: Chart summarizing the different mineral phases observed in each thin section of the different study areas. Qz = Quartz; Kf = Potassium feldspar; Mi = Mica; Ca = Calcite; PPL = Plain-polarized light; XPL = Crossed-polarized light.

| | | Gosau Group sample<br>Poorly sorted arenite | Hecho Group sample<br>Well to poorly sorted arenite | Annot Formation sample<br>Sub-arkose |
|---|---|---|---|---|
| *Naked-eye observed sedimentary structures* | | Structureless and planar-parallel lamination | None / Structureless | Planar-parallel, convolute and ripple -cross lamination |
| *Observed micro-CT characteristics* | | Decrease in low-density particles from base to top<br>Internal structures underlined by low-density particles | Decrease in high-density particles from base to top<br>Internal structures underlined by low-density particles | Dominated by low-density particles<br>Internal structures underlined by high-density particles |
| *Density thresholds (mgHA/ccm$^3$)* | *High-density (HD)* | 1605-2378 (Bulk) | 1453-2378 (Bulk) | 1381-2378 (Internal structures) |
| | *Middle-density (MD)* | 1189-1604 (Bulk) | 1151-1452 (Bulk) | 1071-1380 (Bulk) |
| | *Low-density (LD)* | 423-1188 (Internal structures) | 423-1150 (Internal structures) | 423-1070 (Bulk) |
| *Computed particle -size distribution from micro-CT* | | HD: Mean-grain size = 0.4725 mm<br>Volume fraction = 0.025<br>*Fracture infill*<br>MD: Mean-grain size = 0.3221 mm<br>Volume fraction = 0.7489<br>*No trend (matrix)*<br>LD: Mean-grain size = 0.136 mm<br>Volume fraction = 0.1796<br>*Lamination* | HD: Mean-grain size = 0.1392 mm<br>Volume fraction = 0.2194<br>*Fining upward*<br>MD: Mean-grain size = 0.1928 mm<br>Volume fraction = 0.7399<br>*No trend (matrix)*<br>LD: Mean-grain size = 0.1151 mm<br>Volume fraction = 0.0399<br>*Lamination* | HD: Mean-grain size = 0.0867mm<br>Volume fraction = 0.0186<br>*Lamination*<br>MD: Mean-grain size = 0.1281 mm<br>Volume fraction = 0.5467<br>*No trend*<br>LD: Mean-grain size = 0.1100mm<br>Volume fraction = 0.2738<br>*No trend* |
| *Micro-XRF and chemical element* | | Bulk (matrix) = Mg, Ca, Si<br>Sedimentary structures = Si, K | Bulk (matrix) = Ca, Si, K, Mg | Bulk (matrix) = Si, K, Ca<br>Sedimentary structures = K, Mg, Al |
| *Petrography and computed grain-size from thin-section image analysis* | | Qz, Al-Feld dominant; micritic carbonate (dolomite) matrix, calcite cement<br>Grain size up to 0.5 mm<br>Mean light grain-size = 0.0450 mm<br>Mean dark grain-size = 0.0476 mm | Qz, Feld, calcite dominant; micritic carbonate matrix, calcite cement<br>Grain size up to 1 mm<br>Mean light grain-size = 0.0491 mm<br>Mean dark grain-size = 0.0490 mm | Qz, Feld, mica dominant; calcite minor; poor proportion of fine-grained matrix<br>Grain size up to 0.75 mm<br>Mean light grain-size = 0.0473 mm<br>Mean dark grain-size = 0.0552 mm |

Table 1: Summary table including the detailed results of micro-CT, computed particle-size from micro-CT for each threshold, micro-XRF, petrographic and computed grain-size from thin-section analysis for each sample.

## 4.2 Middle-Eocene Hecho sample

### *Observed micro-CT characteristics*

Micro-CT data from the Eocene Hecho Group (Fig. 8A) shows a general mixture of high- and low-density particles. However, a progressive decrease in the proportion of high-density particles from the base to the top of the sample is noted (Fig. 8B). No particular particle segregation forming internal sedimentary structure is observed. A patch of low-density particles is seen in the middle of the sample, most likely related to some bioturbation.

### *Computed particle-size distribution*

Three density thresholds are identified (Fig. 8C). The category of high-density particles ranges from 1453 to 2378 mgHA/ccm$^3$. It has a mean particle size of 0.1392 mm and a total volume fraction of 0.2194 (Table 1). Particle-size observed in the high-density category shows a progressive decrease from the base to the top of the sample (Fig. 8C), but no particular internal structure is observed (Fig. 8D).

The middle-density particles range from 1151 to 1452 mgHA/ccm$^3$. It shows a mean particle size of 0.1928 mm and a volume fraction of 0.7399 (Table 1). Middle-density particles show an increase in the particle size from the base to the top of the sample (Figs 8C and E). However, this is related to the limits of the algorithm to compute particle-size below silt size (See Discussion section 5.4). No internal structures are observed in this particle-size category (Fig. 8E).

The low-density threshold ranges from 423 to 1150 mgHA/ccm$^3$. It shows a mean particle size of 0.1151 mm and a total volume fraction of 0.0399 (Table 1). As observed in the graph of low-density particle-size variation (Fig. 8C) as well as in the 3D particle-size distribution (Fig. 8F), low-density particles underline internal structures such as millimeterthick planar-parallel lamination at the base of the sample and downflow-cross lamination at the top of the sample (Fig. 8F). A progressive decrease in particle-size is observed from the base to the top of the sample (Fig. 8C).

### *Micro-XRF*

The sample of the Eocene Hecho Group shows a high content in calcium (attributed to calcite from thin section analysis) with a decrease from the base to the top of the sample. Silica (=quartz) is also present throughout the sample (Fig. 8G). There is an increase in the magnesium and potassium content from the base to the top of the sample, attributed to the increase in clay content towards the top of the sample as observed in the thin section. No particular internal sedimentary structure underlined by mineral segregation is observed in the sample.

From alignment between micro-CT and micro-XRF data, calcite grains are related to the highest-density particles of the micro-CT. The middle-density, with the highest volume fraction are related to the carbonate matrix of the sample. Finally, the lowest-density particles are related to the silicate fraction including the quartz and feldspar grains.

### *Petrography and grain-size distribution*

Sandstone sample from the Eocene Hecho Group is classified as an arenite. Although, it cannot be considered as a well-sorted arenite, the degree of sorting is higher than the one observed in the Gosau sample. Main mineral phases consist of quartz, feldspar (alkali feldspar and plagioclase) and carbonate minerals (e.g., calcites and dolomites) (Fig. 7), the latest showing a decrease in its amount towards the top of the sample. Mica and clay flocks are abundant towards the top of the sample. The vertical sorting between silicate and carbonate grains is most likely related to their effective densities and hydrodynamics properties. Grains are sub-angular to sub-rounded. As observed in the Gosau sample, a fine-grained micritic carbonate matrix is filling the gap between grains. Carbonate cements is common surrounding quartz and feldspar minerals. Nummulites are also observed.

From grain-size distribution obtained from thin-section image analysis (Fig. 8I), a progressive decrease in grain-size is observed from the base of the sample to the top. The mean light grain-size and dark grain-size are 0.0491 mm and 0.0490 mm, respectively (Table 1). The base of the sample is structureless whereas some millimeter-scale lamination, most likely related to ripple-cross lamination are observed at the top of the sample.

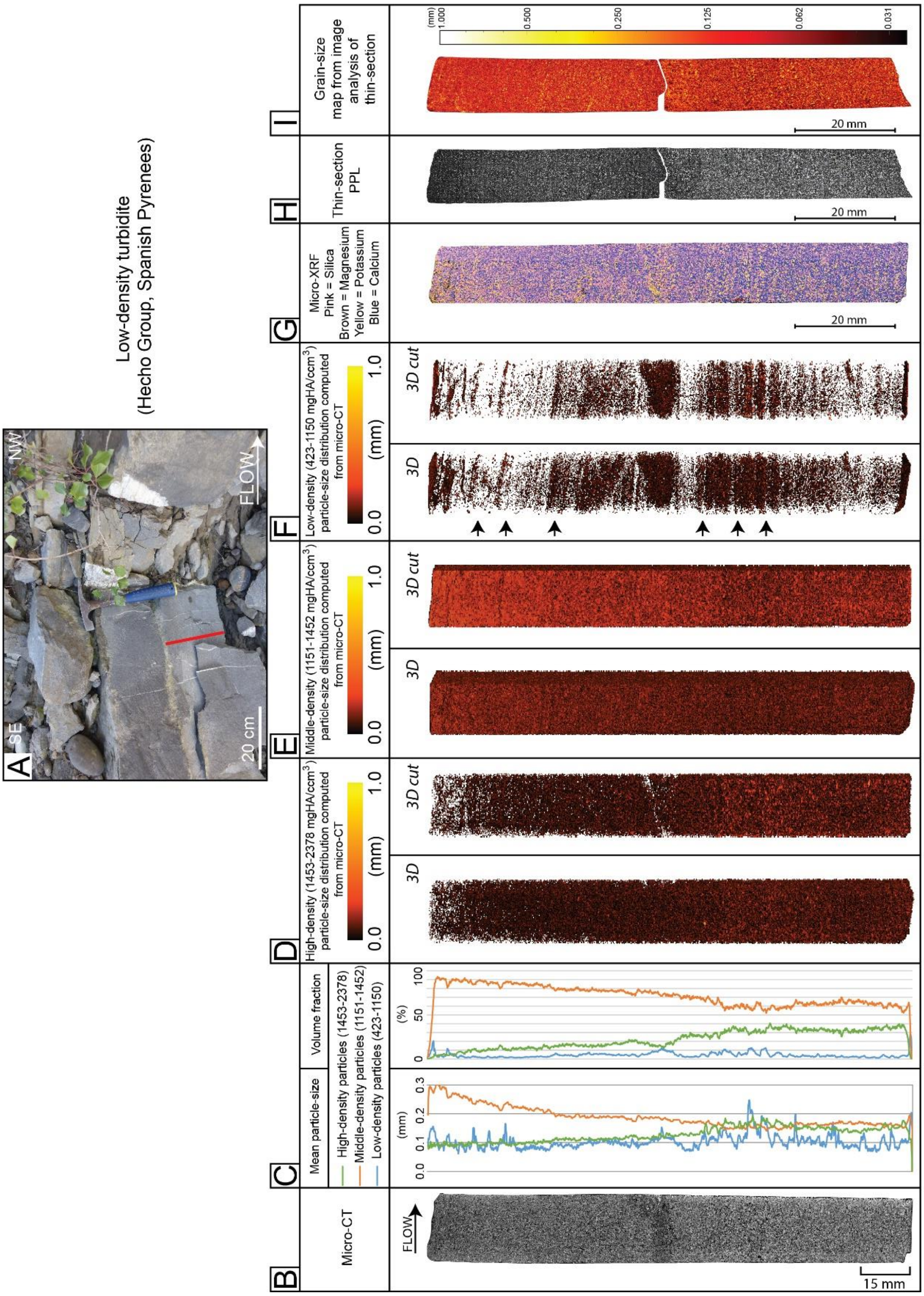


Figure 8: **(A)** Structureless turbidite sampled in the Eocene Hecho Group. **(B)** Native micro-CT image. Dark colors: low-density particle; light colors: high-density particles. **(C)** Graphs illustrating the variations of computed particle-size and volume fraction along the sample for each CT-density threshold. **(D)** Distribution of high-density computed particle-size in 3D and

in a 3D cut parallel to the paleoflow direction. **(E)** Distribution of middle-density computed particle-size in 3D and in a 3D cut parallel to the paleoflow direction. **(F)** Distribution of low-density computed particle-size in 3D and in a 3D cut parallel to the paleoflow direction. Arrows indicate sedimentary structures **(G)** Micro-XRF map. **(H)**Thin-section image (PPL = plain-polarized light). **(I)** Grain-size map computed from thin-section image analysis.

### 4.3 Oligocene Annot Formation sample

***Observed micro-CT characteristics***

Micro-CT image of the Annot Formation sample (Fig. 9A) shows a highest content of low-density particles throughout the sample (Fig. 9B) compared with the Gosau and Hecho samples. Internal structures are underlined by high-density particles. The upper-part of the sample which is the mud cap of the turbidite is represented by a mixture of low- and high-density particles.

***Computed particle-size distribution***

Three density thresholds are identified (Fig. 9C). The high-density threshold is comprised between 1381 to 2378 mgHA/ccm$^3$. The high-density threshold shows the lowest volume fraction throughout the sample with a mean volume fraction of 0.0186. The high-density threshold has the lowest mean particle size of 0.0867 mm (Table 1). The coarsest fraction of the high-density particles is mainly underlying the internal structures of the samples (Fig. 9D), with grain-size above 0.1 mm within the lamination at the base of the sample (Fig. 9C). An increase in the mean grain-size (> 0.1 mm) is observed at the top of the sample, however, this is induced by the presence of clay (mud cap) and the limit of the algorithm computing particle-size in this fine-grained material. Same trends are seen for the middle- and low-density thresholds.

The middle-density threshold (from 1071 to 1380 mgHA/$ccm^3$) has the highest volume fraction in the whole sample with a mean volume fraction of 0.5467, as well as the highest mean particle size with 0.1281 mm (Table 1). Although they are not well visible in the 3D reconstruction in figure 9E, internal structures are characterized by a decrease or an increase in the volume fraction of the middle-density particles, as observed in the graph in figure 9C. As observed in the particle-size graph in figure 9C, the middle density particle-size progressively decreases from the base to the top of the sample. The drastic decrease in the volume fraction at the top of the sample is related to the computing method as particles were analyzed on a square and not on a delimited (with defined boundaries) sample, due to time constrain (at least two additional days of computing). As for the high-density threshold, there is a significant increase in the mean particle-size at the top of the sample (Fig. 9E), due to the limits of the algorithm to compute very-fine particle size (see Discussion section 5.4). From alignment with micro-XRF map, middle-density threshold is most likely related to the fine-grained matrix.

The low-density threshold (from 423-1070 mgHA/$ccm^3$) has a volume fraction of 0.2738 and a mean particle size of 0.11 mm (Table 1). As for the others threshold, significant variation in the volume fraction and particle-size are underlying the internal sedimentary structures (Fig. 9C). As well as the middle-density threshold, the low-density threshold includes the fine-grained matrix.

***Micro-XRF***

Compared to the Gosau and Hecho Group samples, the Annot sample is dominated by silica related to quartz mineral from the base to the top (Fig. 9G). Dark blue/ purple dots scattered throughout the sample (Fig. 9G), are most likely due to the superposition of potassium, silica, and calcium which can be attributed to feldspar (K-feldspar, plagioclase) minerals. Internal structures are underlined by a high content of potassium and magnesium which are attributed to clay minerals (yellow/orange color in figure 9G). This is confirmed by the high content of aluminum observed within the lamination in Supplementary material 1. Both quartz and feldspar are part of the bulk minerals of the sample, whereas laminations are formed by clay segregation. Calcium itself, and hence calcite was not observed in this sample.

By alignment with the micro-XRF, the high-density particles highlighting the lamination are most likely related to the clay minerals. Whereas the low- and middle-density particles are in this case related to the silicate fraction including quartz, feldspar and plagioclase and not showing a strong involvement in the formation of the internal sedimentary structures.

***Petrography and grain-size distribution***

Sandstone sample from the Oligocene Annot formation is categorized as moderately sorted. Its composition can be characterized as a sub-arkose with the main detrital components being Quartz, K-feldspar, and mica (Fig. 7). Although, they are not well detected in micro-XRF. calcite grains are also present and its content decreases from the base to the top of the sample. Compared to the Gosau and Hecho formation, there is a higher proportion of mica minerals and elongated clay minerals, underlying the internal sedimentary structures. A fine-grained matrix is filling the gaps between the grains, however it is in a lower proportion compared to the Gosau and Hecho samples. Calcite cement is present but rare (Fig. 7).

Grain-size calculated from thin section is up to 0.750 mm. Mean light and dark grain-sizes are 0.0473 mm and 0.0552 mm, respectively (Table 1). A progressive fining upward trend is observed from the base to the top of the sample. Some lamination are clearly visible in the computed grain-size map, such as coarse-grained lamination at the base of the sample and few diffuse lamination in the upper part of the sample (Fig. 9I).

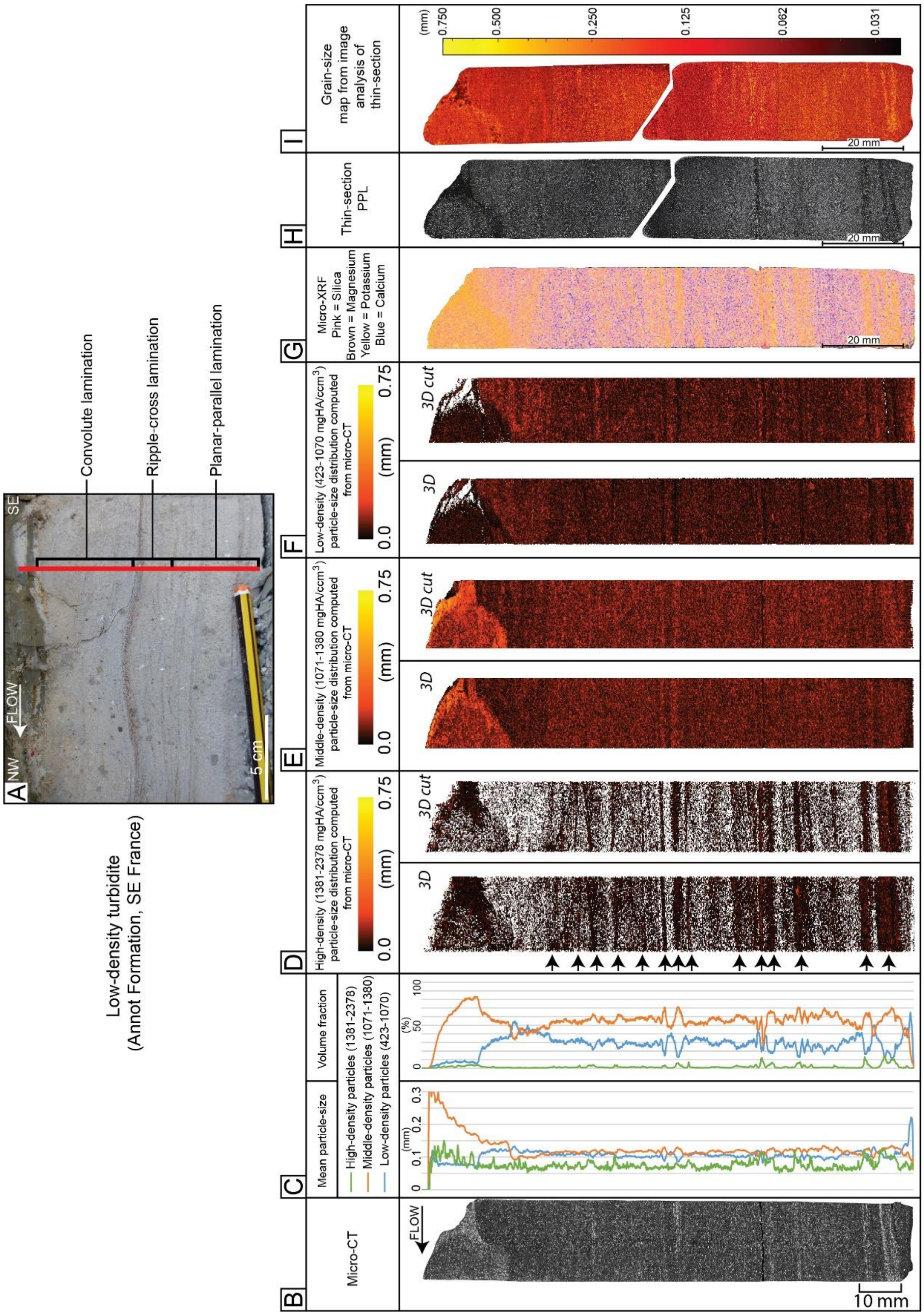


Figure 9: **(A)** Turbidite sampled in the Annot Formation showing planar-parallel lamination overlain by ripple-cross and convolute lamination. **(B)** Native micro-CT image. Dark colors: low-density particle; light colors: high-density particles. **(C)** Graphs illustrating the variations of computed particle-size and volume fraction along the sample for each CT-density threshold.

**(D)** Distribution of high-density computed particle-size in 3D and in a 3D cut parallel to the paleoflow direction. Arrows indicate sedimentary structures **(E)** Distribution of middle-density computed particle-size in 3D and in a 3D cut parallel to the paleoflow direction. **(F)** Distribution of low-density computed particle-size in 3D and in a 3D cut parallel to the paleoflow direction. **(G)** Micro-XRF map. **(H)**Thin-section image (PPL = plain-polarized light). **(I)** Grain-size map computed from thin-section image analysis.

# 5. DISCUSSION

## 5.1 Micro-CT: a new tool to assess and read internal sedimentary structures.

Sedimentary structures, resulting from fluid-particle interaction (e.g., Harms, 1979) have a key role to play in the interpretation of the transport mechanisms of the SGF at the origin of the deposits (e.g., Allen, 1984; Baas et al., 2004). Thus, it is necessary to assess internal sedimentary structures the most accurate possible way to unravel the flow characteristics at the origin of the deposits. As observed in the samples presented in this study, internal sedimentary structures result from grain-size and mineral segregation. Both are closely tied (Picha and Cline, 1973; Collison, 2018) due to the segregation between the coarse-grained detrital materials and the fine-grained matrix, usually, showing contrasting mineral composition. Although one of the limitations of the CT system is to discriminate mineral type (overlap in X-ray attenuation), the X-ray attenuation is enough different to distinguish between the silicate and carbonate fraction. Micro-CT techniques provide the opportunity to isolate particles based on their CT density values. This allows to separate the detrital grains which are commonly the coarsest fraction underlying the sedimentary structures, from the fine-grained matrix showing a different CT signature due to contrasting mineral composition. Although it is valid and observed for all the samples of this study, it is particularly well highlighted in the Gosau sample (Figs. 6D, E and F).

The micro-CT technique is also useful to observe sedimentary structures non-visible with the naked eye in case of too homogeneous deposits in term of mineral composition or grain size. Although no sedimentary structures appear visible due to grain-size segregation, the Hecho sample, rich in carbonate grains and showing a carbonate-rich matrix, sedimentary structures appear to be only visible when isolating the detrital silicate fraction (Fig. 8F). First approach of using CT techniques to study structureless deposits was already conducted by Hamblin (1965), where he detected “micro-cross lamination” in homogeneous sandstones. However, since then, no attention has been carried out to unravel the fabric of structureless deposits. This study brings back into consideration the interpretation of structureless deposits (e.g., Allen, 1971; Hiscott and Middleton, 1980; Patel et al., 2022) observed with the naked eye in the field where more consideration about the mineral composition and grain sorting of the deposits should be done before reaching any interpretation in term of depositional and/or post-depositional processes of structureless deposits. This example shows the significant potential of micro-CT to read sedimentary structures and highlights the possible future application of micro-CT to unravel sedimentary structures non-visible with naked eye in SGF deposits.

## 5.2 Micro-CT vs thin-section in the visualization of internal sedimentary structures

There are many advantages to the use of micro-CT compared with thin-section to analyze internal sedimentary structures : (i) the time of preparation that is relatively short for micro-CT (about 15 min for coring the sample) compared with thin-section (10 to 20 days for thin-section production); (ii) micro-CT scan is considered as a non-destructive method in which structures of the sample are preserved whereas thin-section production can be seen as destructive (e.g., breaking the sample to fit the thin-section size or impregnation preventing subsampling); (iii) possible to observe structures in every direction with micro-CT techniques whereas the plane of thin-sectioning is rarely accurately aligned with the targeted structures which can lead to final misinterpretation; and (iv) the 3D volume and quantification of sandstone component (based on their CT-density phase) computed from micro-CT allowing a better visualization of structures (e.g., Hecho sample), something not possible to obtain from thin-section analysis. This last point is considered as the main advantage of micro-CT. Indeed, the micro-CT technique offers a better visualization of the internal 3D structures of consolidated sandstones than the commonly used 2D characterization tools such as thin-sections with optical microscopy (Davis and Ethridge, 1975; Oren and Bakke, 2002; Asnussen et al., 2015; Bukharev et al., 2018), scanning election microscopy (SEM) (Krinsley et al., 1998; Bera et al., 2011), or simply with the naked eye in the outcrop. Indeed, 2D images, especially 2D thin-section images as presented in this study, do not provide the spatial relationship of sedimentary structures that can be much more complex in 3D (Fig. 10). Direct comparison between thin-section image and isolated 3D micro-CT density threshold images show that sedimentary structures are better visible in selected 3D thresholds than in 2D (Fig. 10). Micro-CT can give good indication on the lamination in 3D and thus on the paleoflow direction or regime (e.g., orientation of cross-lamination), something that could be missed in 2D depending on the 2D view plane. Thus, 2D visualization of sedimentary structures from thin section or by direct observation in outcrop can lead to a limited interpretation of the depositional processes at the origin of the structure.

From the evidences presented, it is clear that 3D imaging by micro-CT techniques has considerable potential within the research of deep-marine sandstones. However, like any technique, it also has limitations (see Section 5.4 for details) and thin sections still provide information that cannot be obtained through micro-CT. Thin-section gives an incomparable resolution of the physical properties within the sedimentary structures, enabling detailed fabric analysis at the grain-to-grain scale (Bendle et al., 2015).

As a consequence, depending on the research target, micro-CT does not represent a stand-alone replacement for thin section analysis in sandstones. Instead, micro-CT should be seen as a reliable companion method, with advantages of being time-saving, non-destructive, and allowing systematic visualization of 3D sedimentary structures. If more details are needed about the grain fabrics or mineral composition forming the internal structures, micro-CT analysis should be complemented by (i) geochemical (e.g., XRF) or mineralogical analyses (e.g., XRD) to associate density thresholds to mineral phase and have a 3D rendered volume of each sandstone component and/or (ii) high-resolution petrographic analysis to get details at the grain scale.

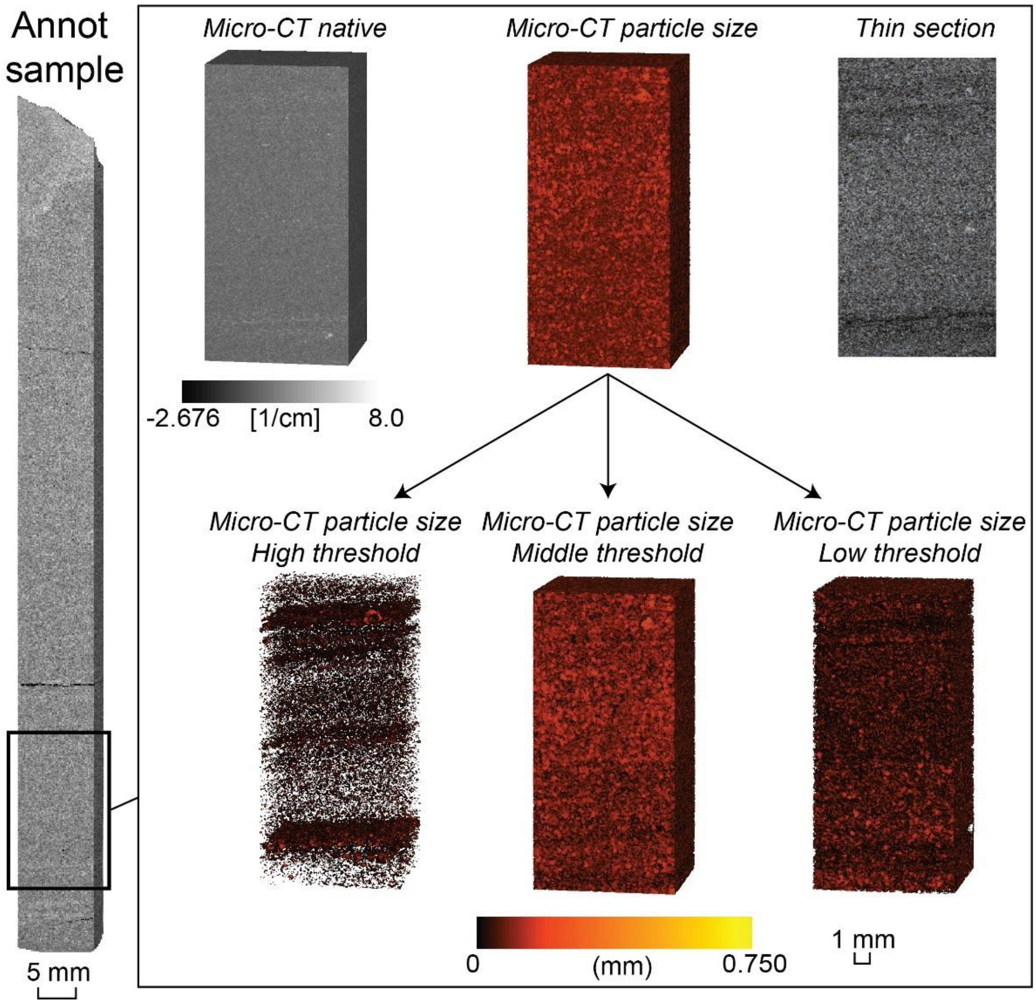


Figure 10: Comparison between the 3D micro CT data and thin-section image based on detailed data selected at the base of the Annot sample. Isolation of the different density thresholds permits a better visualization of the internal sedimentary structures, that are not visible in a 2D thin-section image.

### 5.3 Micro-CT: towards a new tool to evaluate the grain-size distribution

Grain size reflects the energy level of SGFs and is related to the type of SGFs, while sorting is related to the duration of the SGFs (Walker, 1967; Komar, 1985; Hiscott, 1994; Dorrell et al., 2013). Thus, accurate and consistent measure of grain-size distribution in deep-marine sandstones are needed to better understand the processes at its origin. However, the determination of grain-size distribution in consolidated sandstone is problematic. The common sieving technique to measure the grain-size distribution of unconsolidated rocks does not apply efficiently to sandstones. Indeed, after disaggregation of cemented sandstones, the presence of broken grains or grain aggregates will result in a cumulative curve. Until now, grain-size analysis of consolidated sandstones is mainly based on point counting techniques in thin-section (e.g., Ingersoll et al., 1984; Stevenson et al., 2020) or by image analysis of thin-section (e.g., Schafer and Teyssen, 1987; Hüneke et al., 2021). Although the use of thin-section analysis to measure grain-size is valuable, a remaining debate subsist related to the measurement of random sections through grains (apparent size) rather than their actual dimensions (true size) (e.g., Johnson, 1994; Buscombe, 2013), leading to a lack of consistency in the analysis of grain-size distribution (Fig. 11). Furthermore, grain-size is measured only on a 2D plan and thus there a deficit of information in 3D from thin-section analysis.

In Earth Science, measuring grain-size based on X-CT data is not new as it has already been tested on ore deposits (Evans et al., 2015), individual targeted grains (e.g., apatite, Cooperdock et al., 2019) or on sediment-core samples (Orru et al., 2012). However, until now, the grain-size measurement from micro-CT data of consolidated sandstone samples has not been presented. Thanks to the development of a bubble growing algorithms (Hildebrand and Rüeggsegger, 1997), particle-size measurement from micro-CT sandstone data is possible. One advantage of measuring the particle size from micro-CT data compared with grain-size measurement from thin section, is related to the consistency of the results (Fig. 11). Indeed, from micro-CT data, the same axis (short axis in this study) for each particle is measured thanks to the visualization in 3D. The consistent particle-size measurement and the 3D visualization given by the micro-CT will, *in fine*, leads towards more reliable models of particle-size distribution and thus more accurate interpretations.

If we directly compare the grain-size maps obtained by image analysis of thin-section and the particle-size images computed from micro-CT data, grains and particles show similar distribution on the three samples (see figs. 6B, 8B, 9B with grain-size map for each sample), testifying of the reliability of particle-size measurement from micro-CT data. However, if the mean grain-size for each type of grain class is compared to the mean particle-size computed for each micro-CT density thresholds, some divergences arise. Indeed, mean grain-size shows value of one tenth lower than computed mean particle size (Table 1). This is certainly related to the combination of (1) the limitation of micro-CT algorithm to compute particle-size below the silt size and resulting in cluster of silt-particles showing coarser size than the actual dimensions; with (2) the selection of very-small size particle within the matrix (artefact; difficulties to isolate the very-fine grains from the matrix) during image segmentation of thin-section pictures.

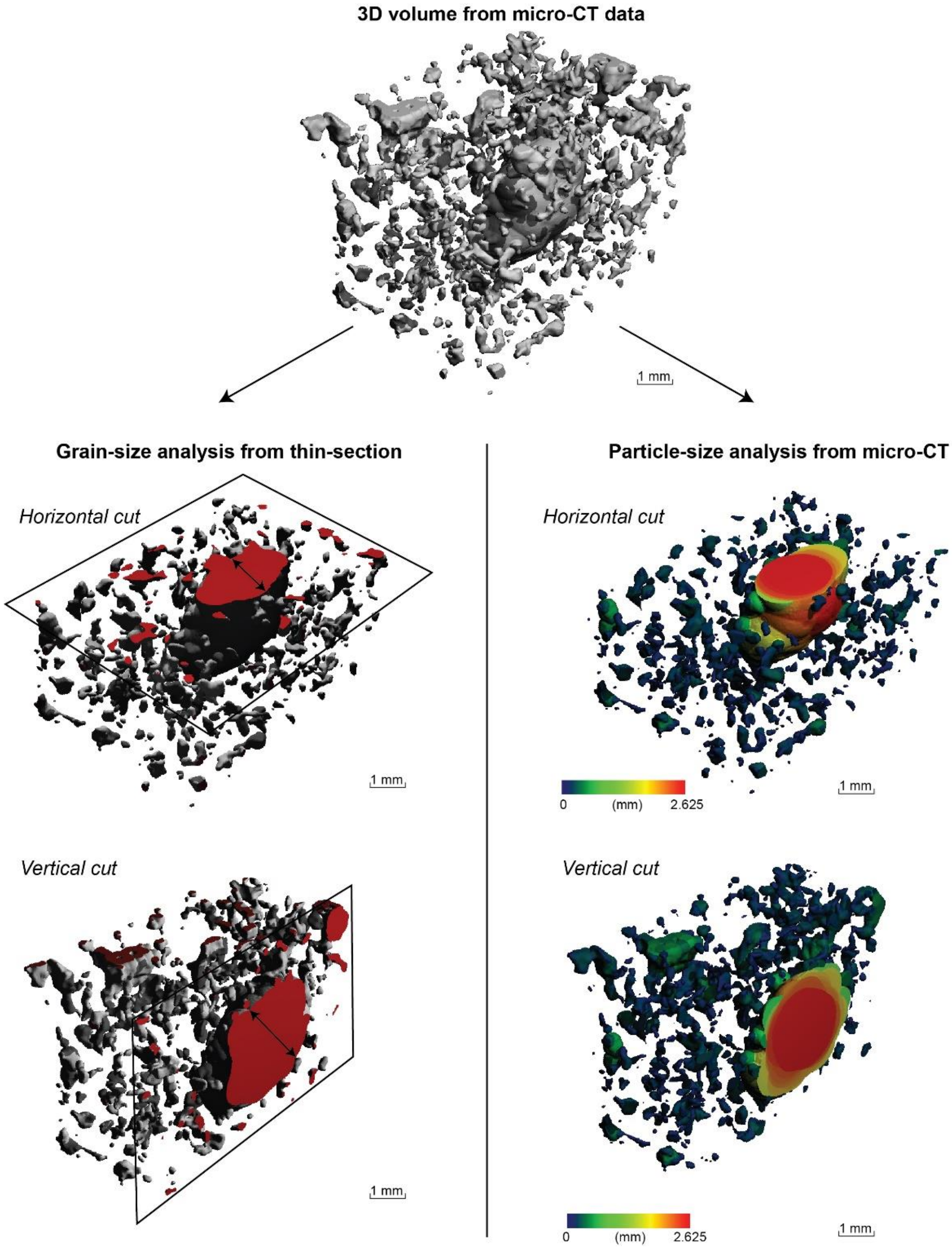


Figure 11: Illustration of the differences between grain-size computed from thin section (left column) and particle-size computed from micro-CT data (right column). Depending on the cutting plane of the thin section (here horizontal *vs* vertical), the short axis of a grain does not have the same value. Whereas particle-size computed from micro-CT data, show same value for the short axis in every direction, thus giving more consistent particle-size measurement than grain-size measurement from thin sections. Example taken from a sample collected on a turbidite from the Hecho Group.

### 5.4. Limitations of the described algorithm and micro-CT

The maximum theoretical resolution with the used micro-CT setup is 10.5 µm. However, in order to improve the image quality and thus the segmentation results, hardware binning was implemented, leading to a reduced voxel size of 21 µm. This impacts directly on the resolvable grain size leading to the fact that (i) grains near the resolution border tend to be overestimated and (ii) grains below the resolution border will be considered as interconnected particle. This is well highlighted in the three samples of this study, where the fine-grained matrix shows the highest mean particle size, as also discussed in further details by Elkhoury et al. (2019).

Until now, another limitation of the used algorithm is that no individual grain can be distinguished because of the inability to detect the boundaries between touching grains of the same CT density. This also prevents to measure grain orientation. In the future, potential solutions to distinguish individual grains would be to implement and test 3D watershed methods.

Due to the usage of a conventional X-ray source, only a tendency in mineral composition can be observed in the micro-CT images. The potential of using synchrotron x-ray radiation may lead to higher contrast between mineral phases. Although synchrotron micro-CT has its potential, availability and costs are a discriminating factor.

### 5.5 Wider implications for consolidated sandstones

As shown by this study, micro-CT technique is a new and excellent tool to better visualize the primary (depositional) fabric of sandstones providing a better assessment of internal sedimentary structures (including the ones non-visible with the naked eye) and a consistent appraisal of grain-size distribution. Fabric development is directly linked to the paleohydraulic conditions of the SGF during deposition (Middleton, 1965; Allen, 1970; Arnott and Hand, 1989; Baas, 2004; Sumner et al., 2008; Talling, 2013). Thus, micro-CT would be a very valuable tool helping in the reconstruction of the flow characteristics at the origin of the deep-marine sandstone beds such as waning vs waxing flows, traction vs non-traction dominated flows, or the flow regime (upper- vs lower-flow regime; Cornard and Pickering, 2019). The opportunity of computing the volume of the coarse-grained fraction vs fine-grained (matrix) fraction could also give a more accurate interpretation on the type of deposits and related processes (matrix-rich vs matrix-poor sandstones; e.g., Terlaky and Arnott, 2013).

The development of sandstone fabrics, in the form of texturally or mineralogically, is almost universally similar in the sedimentary realm. Thus, the fabric assessment of consolidated sandstones by micro-CT technique is not restricted to deep-marine sandstones but can also be applied to sandstones from different depositional environment such as shallow-marine, fluvial or glaciogenic environments.

The application of micro-CT techniques on outcrop data, in which the lateral extent allows trustworthy interpretation of paleoflow conditions (e.g., bedform), permits the development of micro-proxies of the internal fabrics. These proxies would be interesting to apply to core data where the poor lateral extent prevent any reliable interpretation of the paleoflow conditions at the time of deposition.

## 6. CONCLUSIONS

This study explores the potential of micro-CT techniques to read sedimentary structures in deep-marine sandstones. Because of the importance of the mineral composition in the formation and preservation of sedimentary structures, micro-CT analysis are complemented by geochemical analysis based on micro-XRF mapping and petrographic analysis involving thin-section analysis. This multi-disciplinary approach is tested on three samples showing different mineral composition: a poorly sorted arenite from the Gosau Group in the Muttekopf Basin (Austria); a well to poorly sorted arenite from the Hecho Group in the Ainsa Basin (Spain); and a sub-arkose collected in the Annot Formation (France).

By comparing grain-size measurement from thin-section image analysis, micro-CT data shows itself valuable data to compute particle-size. The reconstruction of the particle-size distribution permits a better visualization of the sedimentary structures in 3D. By isolating particles based on their CT-density, it is possible to separate the coarsest (detrital) fraction underlying the sedimentary structures from the fine-grained matrix. This technique is very valuable to visualize sedimentary structures that are not visible with the naked eye, in case of too homogeneous deposit composition, in term of grain size and mineralogy. This study brings back the evaluation of structureless deposits in the outcrop, and the importance of evaluating the mineral composition and grain sorting before to reach any interpretation in term of process at the origin of the deposits.

Compare to 2D thin-section analysis, they are many advantages to use micro-CT to analyze internal sedimentary structures, it is a non-destructive and time-saving techniques as well as allowing a systematic visualization of 3D sedimentary structures. Because of the limitation of micro-CT to measure below silt size, companion methods such as geochemical or high-resolution petrographic analyses are needed to get more information about the grain fabric at the grain-to-grain scale or mineral composition.

Micro-CT is an innovative tool to better visualize primary sedimentary structures of consolidated SGF deposits, and thus an excellent technique to include in the reconstruction of paleoflow condition and depositional processes at the origin of the deposits. Because the formation of sandstone fabrics is almost universal in the sedimentary realm, micro-CT will also help to give a better assessment of sedimentary structures and associated processes at their origin, in different types of depositional environments (e.g., fluvial, shallow-marine). Considering the importance of the sedimentary structures visualization in the interpretation of the processes at the origin of the deposits, micro-CT is a reliable tool to assess the physical properties responsible for the deposition of ancient deposits.


## ACKNOWLEDGEMENTS

Pauline Cornard is funded by the FWF Austrian Science Fund (Flow-Dynamic-Fan project M3065N). Simon Wagner is thanked for his help with micro-XRF analysis.


## REFERENCES


Allen, J. R. L. (1970). A quantitative model of grain size and sedimentary structures in lateral deposits. *Geological Journal*, 7(1), 129–146.

Allen, J. R. L. (1971). Massive beds in the central Pennine Basin: a discussion. *Proceedings of the Yorkshire Geological Society*, 38(2), 293–294.

Arnott, R. W. C., and Hand, B. M. (1989). Bedforms, primary structures and grain fabric in the presence of suspended sediment rain. *Journal of Sedimentary Research*, 59(6), 1062–1069.

Asmussen, P., Conrad, O., Günther, A., Kirsch, M., and Riller, U. (2015). Semi-automatic segmentation of petrographic thin section images using a “seeded-region growing algorithm” with an application to characterize wheathered subarkose sandstone. *Computers & Geosciences*, 83, 89–99.

Baas, J. H. (2004). Conditions for formation of massive turbiditic sandstones by primary depositional processes. *Sedimentary Geology*, 166(3-4), 293–310.

Bam, L. C., Miller, J. A., and Becker, M. (2020). A mineral X-ray linear attenuation coefficient tool (MXLAC) to assess mineralogical differentiation for X-ray computed tomography scanning. *Minerals*, 10(5), 441.

Baraka-Lokmane, S., Main, I. G., Ngwenya, B. T., and Elphick, S. C. (2009). Application of complementary methods for more robust characterization of sandstone cores. *Marine and Petroleum Geology*, 26(1), 39–56.

Best, J. I. M., and Bridge, J. (1992). The morphology and dynamics of low amplitude bedwaves upon upper stage plane beds and the preservation of planar laminae. *Sedimentology*, 39(5), 737–752.

Bera, B., Mitra, S. K., and Vick, D. (2011). Understanding the micro structure of Berea Sandstone by the simultaneous use of micro-computed tomography (micro-CT) and focused ion beam-scanning electron microscopy (FIB-SEM). *Micron*, 42(5), 412–418.

Bertels, S. P., DiCarlo, D. A., and Blunt, M. J. (2001). Measurement of aperture distribution, capillary pressure, relative permeability, and in situ saturation in a rock fracture using computed tomography scanning. *Water Resources Research*, 37(3), 649–662.

Boone, M., Dewanckele, J., Boone, M., Cnudde, V., Silversmit, G., Van Ranst, E., et al. (2011). Three-dimensional phase separation and identification in granite. *Geosphere*, 7(1), 79–86.

Bukharev, A. Y., Budennyy, S. A., Pachezhertsev, A. A., Belozerov, B. V., and Zhuk, E. A. (2018, September). Automatic analysis of petrographic thin section images of sandstone. In ECMOR XVI-16th European Conference on the Mathematics of Oil Recovery (Vol. 2018, No. 1, pp. 1-10). European Association of Geoscientists & Engineers.

Buscombe, D. (2013). Transferable wavelet method for grain-size distribution from images of sediment surfaces and thin sections, and other natural granular patterns. *Sedimentology*, 60(7), 1709–1732.

Campbell, C. V. (1967). Lamina, laminaset, bed and bedset. *Sedimentology*, 8(1), 7–26.

Carlson, W. D. (2006). Three-dimensional imaging of earth and planetary materials. *Earth and Planetary Science Letters*, 249(3-4), 133–147.

Cartigny, M. J., Eggenhuisen, J. T., Hansen, E. W., and Postma, G. (2013). Concentration-dependent flow stratification in experimental high-density turbidity currents and their relevance to turbidite facies models. *Journal of Sedimentary Research*, 83(12), 1047–1065.

Cheel, R. J. (1990). Horizontal lamination and the sequence of bed phases and stratification under upper-flow-regime conditions. *Sedimentology*, 37(3), 517–529.

Cnudde, V., Boone, M., Dewanckele, J., Dierick, M., Van Hoorebeke, L., and Jacobs, P. (2011). 3D characterization of sandstone by means of X-ray computed tomography. *Geosphere*, 7(1), 54–61.

Cnudde, V., and Boone, M. N. (2013). High-resolution X-ray computed tomography in geosciences: A review of the current technology and applications. *Earth-Science Reviews*, 123, 1–17.

Coenen, J., Tchouparova, E., and Jing, X. (2004). Measurement parameters and resolution aspects of micro X-ray tomography for advanced core analysis. In proceedings of International Symposium of the Society of Core Analysts.

Collinson, J. (2019). Sedimentary structures. Dunedin Academic Press Ltd.

Cooperdock, E. H., Ketcham, R. A., and Stockli, D. F. (2019). Resolving the effects of 2-D versus 3-D grain measurements on apatite (U–Th) ∕ He age data and reproducibility. *Geochronology*, 1(1), 17–41.

Cornard, P. H., & Pickering, K. T. (2019). Supercritical-flow deposits and their distribution in a submarine channel system, middle Eocene, Ainsa Basin, Spanish Pyrenees. *Journal of Sedimentary Research*, 89(6), 576–597.

Davies, D. K., and Ethridge, F. G. (1975). Sandstone composition and depositional environment. *AAPG Bulletin*, 59(2), 239–264.

Dorrell, R. M., Hogg, A. J., and Pritchard, D. (2013). Polydisperse suspensions: Erosion, deposition, and flow capacity. *Journal of Geophysical Research: Earth Surface*, 118(3), 1939–1955.

Elkhoury, J. E., Shankar, R., and Ramakrishnan, T. S. (2019). Resolution and limitations of X-ray micro-CT with applications to sandstones and limestones. *Transport in Porous Media*, 129(1), 413-425.

Evans, C. L., Wightman, E. M., and Yuan, X. (2015). Quantifying mineral grain size distributions for process modelling using X-ray micro-tomography. *Minerals Engineering*, 82, 78–83.

Falvard, S., and Paris, R. (2017). X-ray tomography of tsunami deposits: Towards a new depositional model of tsunami deposits. *Sedimentology*, 64(2), 453–477.

Feldkamp, L. A., Goldstein, S. A., Parfitt, M. A., Jesion, G., and Kleerekoper, M. (1989). The direct examination of three-dimensional bone architecture in vitro by computed tomography. *Journal of bone and mineral research*, 4(1), 3–11.

Ghorbani, Y., Becker, M., Petersen, J., Morar, S. H., Mainza, A., and Franzidis, J. P. (2011). Use of X-ray computed tomography to investigate crack distribution and mineral dissemination in sphalerite ore particles. *Minerals Engineering*, 24(12), 1249–1257.

Hamblin, W. K. (1965). Internal structures of" homogeneous" sandstones (Vol. 175). University of Kansas.

Harms, J. C. (1979). Primary sedimentary structures. *Annual Review of Earth and Planetary Sciences*, 7, 227.

Hildebrand, T. and Rüegsegger, P. (1997). A new method for the model-independent assessment of thickness in three-dimensional images. *Journal of Microscopy*, 185, 67-75.

Hiscott, R. N. (1994). Loss of capacity, not competence, as the fundamental process governing deposition from turbidity currents. *Journal of Sedimentary Research*, 64(2a), 209–214.

Hiscott, R. N., and Middleton, G. V. (1980). Fabric of coarse deep-water sandstones, Tourelle Formation, Quebec, Canada. *Journal of Sedimentary Research*, 50(3), 703–721.

Hüneke, H., Hernández-Molina, F. J., Rodríguez-Tovar, F. J., Llave, E., et al., (2021). Diagnostic criteria using microfacies for calcareous contourites, turbidites and pelagites in the Eocene–Miocene slope succession, southern Cyprus. *Sedimentology*, 68(2), 557–592.

Ingersoll, R. V., Bullard, T. F., Ford, R. L., Grimm, J. P., Pickle, J. D., & Sares, S. W. (1984). The effect of grain size on detrital modes: a test of the Gazzi-Dickinson point-counting method. *Journal of Sedimentary Research*, 54(1), 103–116.

Jerram, D. A., Mock, A., Davis, G. R., Field, M., and Brown, R. J. (2009). 3D crystal size distributions: A case study on quantifying olivine populations in kimberlites. *Lithos*, 112, 223–235.

Jiang, Z. (1995). The motion of sediment-water mixtures during intense bedload transport: computer simulations. *Sedimentology*, 42(6), 935–945.

Johnson, M. R. (1994). Thin section grain size analysis revisited. *Sedimentology*, 41(5), 985–999.

Ketcham, R. A., and Carlson, W. D. (2001). Acquisition, optimization and interpretation of X-ray computed tomographic imagery: applications to the geosciences. *Computers & Geosciences*, 27(4), 381–400.

Kim, K. Y., Zhuang, L., Yang, H., Kim, H., and Min, K. B. (2016). Strength anisotropy of Berea sandstone: results of X-ray computed tomography, compression tests, and discrete modeling. *Rock Mechanics and Rock Engineering*, 49(4), 1201–1210.

Kiminami, K., and Kontani, Y. (1979). Pre-Cretaceous paleocurrents of the northeastern Hidaka belt, Hokkaido, Japan. 北海道大学理学部紀要, 19(1-2), 179–188.

Komar, P.D. (1989). The hydraulic interpretation of turbidites from their grain sizes and sedimentary structures. *Sedimentology*, 32, 396–407.

Krinsley, D. H., Pye, K., Boggs Jr, S., & Tovey, N. K. (1998). Backscattered scanning electron microscopy and image analysis of sediments and sedimentary rocks. Cambridge University Press.

Kuenen, P. H. (1966). Experimental turbidite lamination in a circular flume. *The Journal of Geology*, 74, 523–545.

Kumari, W. G. P., Ranjith, P. G., Perera, M. S. A., Li, X., Li, L. H., et al. (2018). Hydraulic fracturing under high temperature and pressure conditions with micro CT applications: geothermal energy from hot dry rocks. *Fuel*, 230, 138–154.

Kyle, J. R., and Ketcham, R. A. (2015). Application of high resolution X-ray computed tomography to mineral deposit origin, evaluation, and processing. *Ore Geology Reviews*, 65, 821–839.

Legros, F. (2002). Can dispersive pressure cause inverse grading in grain flows?. *Journal of Sedimentary Research*, 72(1), 166–170.

Lei, L., Seol, Y., Choi, J. H., and Kneafsey, T. J. (2019). Pore habit of methane hydrate and its evolution in sediment matrix–Laboratory visualization with phase-contrast micro-CT. *Marine and Petroleum Geology,* 104, 451–467.

McCoy, T. J., Ketcham, R. A., Wilson, L., Benedix, G. K., Wadhwa, M., and Davis, A. M. (2006). Formation of vesicles in asteroidal basaltic meteorites. *Earth and Planetary Science Letters*, 246(1-2), 102–108.

Middleton, G. V. (1965). Primary sedimentary structures and their hydrodynamic interpretation. *SEPM Special Publication* N 12.

Munkholm, L. J., Heck, R. J., and Deen, B. (2012). Soil pore characteristics assessed from X-ray micro-CT derived images and correlations to soil friability. *Geoderma,* 181, 22–29.

Mutti, E. (1977), Distinctive thin-bedded turbidite facies and related depositional environments in the Eocene Hecho Group (south-central Pyrenees, Spain). *Sedimentology,* 24, 107–131.

Nelson, H.M., Flemings, P.B., Germaine, J.T., and Dugan, B.E. (2009). Data report: radiography and X-ray CT imaging of whole core from IODP Expedition 308, Gulf of Mexico. In Flemings, P.B., Behrmann, J.H., John, C.M., and the Expedition 308 Scientists, Proc. IODP, 308: College Station, TX. (Integrated Ocean Drilling Program Management International, Inc.)

Øren, P. E., and Bakke, S. (2002). Process based reconstruction of sandstones and prediction of transport properties. *Transport in porous media*, 46(2), 311–343.

Orru, C., Blom, A., and Uijttewaal, W. (2012). Laboratory measurements to determine the grain size distribution of a sand-gravel bed surface and substrate: image analysis and CT scanner analysis. In AGU Fall Meeting Abstracts (Vol. 2012, EP53B-1026).

Orsi, T. H., Edwards, C. M., and Anderson, A. L. (1994). X-ray computed tomography: a nondestructive method for quantitative analysis of sediment cores. *Journal of Sedimentary Research*, 64(3).

Otani, J., Watanabe, Y., and Chevalier, B. (2010). Introduction of X-ray CT application in geotechnical engineering–theory and practice. In IOP Conference Series: Materials Science and Engineering (10, 012089). IOP Publishing.

Ortner, H. (2001). Growing folds and sedimentation of the Gosau Group, Muttekopf, Northern Calcareous Alps, Austria. *International Journal of Earth Sciences*, 90(3), 727–739.

Ortner, H., Kositz, A., Willingshofer, E., and Sokoutis, D. (2016). Geometry of growth strata in a transpressive fold belt in field and analogue model: Gosau Group at Muttekopf, Northern Calcareous Alps, Austria. *Basin Research*, 28(6), 731–751.

Paola, C., Wiele, S. M., and Reinhart, M. A. (1989). Upper-regime parallel lamination as the result of turbulent sediment transport and low-amplitude bed forms. *Sedimentology*, 36, 47–59.

Patel, U. S., Stow, D. A., Gardiner, A., and Buckman, J. (2022). Textual heterogeneity in massive sandstones from the Grès d'Annot and Numidian Flysch: Implications for depositional processes. *Journal of Sedimentary Research*, 92(4), 321-352.

Penkrot, M. L., Jaeger, J. M., Cowan, E. A., St-Onge, G., and LeVay, L. (2018). Multivariate modeling of glacimarine lithostratigraphy combining scanning XRF, multisensory core properties, and CT imagery: IODP Site U1419. *Geosphere*, 14, 1935–1960.

Picha, F., and Cline, L. M. (1973). Radiographic investigation of laminated and ripple cross-laminated flysch sandstones, Ouachita Mountains, Oklahoma. *Journal of Sedimentary Research*, 43(2).

Pickering, K. T., and Hilton, V. C. (1998). Turbidite systems of southeast France: Application to hydrocarbon prospectivity. Vallis Press.

Pickering, K. T., and Hiscott, R. N. (2016). Deep Marine Systems. Processes, Deposits, Environments, Tectonics and Sedimentation, AGU and Wiley.

Polacci, M., Mancini, L., and Baker, D. R. (2010). The contribution of synchrotron X-ray computed microtomography to understanding volcanic processes. *Journal of synchrotron radiation*, 17, 215–221.

Rüegsegger, P., Koller, B., & Müller, R. (1996). A microtomographic system for the nondestructive evaluation of bone architecture. *Calcified tissue international*, 58(1), 24–29.

Sabatier, P., Moernaut, J., Bertrand, S., Van Daele, M., Kremer, K., Chaumillon, E., and Arnaud, F. (2022). A review of event deposits in lake sediments. *Quaternary*, 5(3), 34.

Schäfer, A., and Teyssen, T. (1987). Size, shape and orientation of grains in sands and sandstones—image analysis applied to rock thin-sections. *Sedimentary Geology*, 52(3-4), 251–271.

Schmitt, M., Halisch, M., Müller, C., and Fernandes, C. P. (2016). Classification and quantification of pore shapes in sandstone reservoir rocks with 3-D X-ray micro-computed tomography. *Solid Earth*, 7(1), 285–300.

Siddiqui, S., Funk, J. J., and Al-Tahini, A. M. (2010). Use of X-ray CT to measure pore volume compressibility of Shaybah carbonates. *SPE Reservoir Evaluation & Engineering*, 13(01), 155–164.

Singh, N., Kumar, S., Udawatta, R. P., Anderson, S. H., de Jonge, L. W., and Katuwal, S. (2021). X-ray micro-computed tomography characterized soil pore network as influenced by long-term application of manure and fertilizer. *Geoderma*, 385, 114872.

Sleutel, S., Cnudde, V., Masschaele, B., Vlassenbroek, J., Dierick, M., Van Hoorebeke, L., et al., (2008). Comparison of different nano-and micro-focus X-ray computed tomography set-ups for the visualization of the soil microstructure and soil organic matter. *Computers & Geosciences*, 34(8), 931–938.

Sok, R. M., Knackstedt, M. A., Varslot, T., Ghous, A., Latham, S., and Sheppard, A. P. (2010). Pore scale characterization of carbonates at multiple scales: Integration of Micro-CT, BSEM, and FIBSEM. *Petrophysics - The SPWLA Journal of Formation Evaluation and Reservoir Description*, 51(06).

Su, Y., Zha, M., Jiang, L., Ding, X., Qu, J., Jin, J., and Iglauer, S. (2022). Pore structure and fluid distribution of tight sandstone by the combined use of SEM, MICP and X-ray micro-CT. *Journal of Petroleum Science and Engineering*, 208, 109241.

Stevenson, C. J., Peakall, J., Hodgson, D. M., Bell, D., & Privat, A. (2020). TB or not TB: banding in turbidite sandstones. *Journal of Sedimentary Research*, 90(8), 821–842.

Stow, D. A. V., & Piper, D. J. W. (1984). Deep-water fine-grained sediments: facies models. *Geological Society, London, Special Publications*, 15(1), 611–646.

Sumner, E. J., Amy, L. A., and Talling, P. J. (2008). Deposit structure and processes of sand deposition from decelerating sediment suspensions. *Journal of Sedimentary Research*, 78(8), 529–547.

Talling, P. J. (2013). Hybrid submarine flows comprising turbidity current and cohesive debris flow: Deposits, theoretical and experimental analyses, and generalized models. *Geosphere*, 9(3), 460–488.

Terlaky, V., and Arnott, R. W. C. (2014). Matrix-rich and associated matrix-poor sandstones: avulsion splays in slope and basin-floor strata. *Sedimentology*, 61(5), 1175–1197.

Tiwari, P., Deo, M., Lin, C. L., and Miller, J. D. (2013). Characterization of oil shale pore structure before and after pyrolysis by using X-ray micro CT. *Fuel*, 107, 547–554.

Van Daele, M., Cnudde, V., Boone, M., Deprez, M., and De Batist, M. (2016l). On how X-ray (micro) computed tomography on turbidites can help us unravel paleoflow successions, directions and dynamics. In EGU General Assembly Conference Abstracts (pp. EPSC2016-12825).

Vergés, J., Fernàndez, M. and Martínez, A. (2002). The Pyrenean orogen: pre-, syn-, and post-collisional evolution. In: Rosenbaum, G. and Lister, G. S., 2002. Reconstruction of the evolution of the Alpine-Himalayan orogeny. *Journal of the Virtual Explorer*, 8, 57–76.

Walker, R. G. (1967). Turbidite sedimentary structures and their relationship to proximal and distal depositional environments. *Journal of Sedimentary Research*, 37(1), 25–43.

Wagreich, M., and Faupl, P. (1994). Palaeogeography and geodynamic evolution of the Gosau Group of the northern Calcareous Alps (Late Cretaceous, eastern Alps, Austria). *Palaeogeography, Palaeoclimatology, Palaeoecology*, 110(3-4), 235–254.

Wildenschild, D., and Sheppard, A. P. (2013). X-ray imaging and analysis techniques for quantifying pore-scale structure and processes in subsurface porous medium systems. *Advances in Water resources*, 51, 217–246.

Wils, K., Deprez, M., Kissel, C., Vervoort, M., Van Daele, M., Daryono, M. R., et al. (2021). Earthquake doublet revealed by multiple pulses in lacustrine seismo-turbidites. *Geology*, 49(11), 1301–1306.

Yang, S. Q., Yang, Z., Jing, H. W., and Xu, T. (2020). Fracture evolution mechanism of hollow sandstone under conventional triaxial compression by X-ray micro-CT observations and three-dimensional numerical simulations. *International Journal of Solids and Structures*, 190, 156–180.

**Supplementary Material 1**

Micro-XRF images of the Gosau, Hecho and Annot samples. The left micro-XRF image of each sample displays the following chemical elements: Aluminum (Al in blue), Silica (Si in green) and Calcium (Ca in orange). By layering these chemical elements, the following mineral phases are interpreted: feldspar and clay in blue, quartz in green, carbonate minerals in orange. The right micro-XRF image of each sample displays the following chemical elements: Magnesium (Mg in brown), Potassium (K in yellow), Calcium (Ca in Blue). By layering these chemical elements, the following mineral phases are interpreted: feldspar in yellow, dolomite in purple/pink, calcite in blue, clay in orange, quartz in black.